Tunable Band Gaps of Nanocrystals Encapsulated by the Protein Ferritin

Stephen Dale Erickson

A senior thesis submitted to the faculty of
Brigham Young University
in partial fulfillment of the requirements for the degree of

Bachelor of Science

Dr. John Colton, Advisor

Department of Physics and Astronomy

Brigham Young University

April 2015

ABSTRACT

Tunable Band Gaps of Nanocrystals Encapsulated by the Protein Ferritin

Stephen Dale Erickson
Department of Physics and Astronomy, BYU
Bachelor of Science

Nanostructured solar cells seek to surpass the present standards of efficiency and affordability in solar energy. The protein ferritin—a 12 nm diameter hollow sphere—serves as a unique template for synthesizing nanoscale solar energy materials. It allows for controlled and uniform nanocrystal synthesis, protection against photo-corrosion, and the ability to be manipulated into ordered arrays. In this thesis, I present a method of tuning the band gap of these encapsulated nanocrystals over a range of 1.60-2.38 eV by controlling their size and chemical composition during synthesis. Band gaps are measured using optical absorption spectroscopy to test the effects of these tunable parameters. Using just these materials, calculations indicate that the maximum solar energy conversion efficiencies under average sunlight could reach a high value of 38.0%. The addition of a material with a band gap similar to silicon (1.12 eV) would raise this maximum efficiency to 51.3%.

Keywords: nanocrystals, quantum dots, ferritin, band gaps, photovoltaics

ACKNOWLEDGMENTS

None of the work that went into this thesis would have been possible without the help and support of those around me. First, I am indebted to Scott Panik for sparking my initial interest in physics and giving me an excellent foundation to begin my studies at Brigham Young University. Next, I would especially like to thank my advisor, Dr. John Colton, for his endless counsel, patience, and for giving me the opportunity to research in his lab. I would also like to thank Dr. Richard Watt, Trevor Smith, Jacob Embly, and Cameron Olsen for synthesizing all of my samples and performing the relevant chemical analysis. Various sources of funding made this work possible. My thanks go out to the Utah Office of Energy Development, NSF REU program, and the BYU Department of Physical and Mathematical Sciences for funding this project. Finally, I thank Brook for her support throughout this project and as we dive into the future.

Contents

List of Figures

List of Tables

Chapter 1

Introduction

1.1 Overview of Thesis

Limited fossil fuel reserves and environmental concerns over their use has driven recent expansion in the field of solar energy. While significant progress has been made, innovation is needed to avoid impending barriers. Quantum dot solar cells seek to revolutionize this field, bringing several benefits unavailable to their bulk state counterparts, such as tunable band gaps and multi-excitation events. Ferritin-encapsulated nanocrystals offer additional benefits over traditional quantum dot solar cells, like protection from photo-corrosion and the ability to control their arrangement, making them a strong candidate for harvesting solar energy.

The goal of this research project is to characterize the band gaps of nanocrystals encapsulated by the spherical protein shell ferritin and investigate how the band gap can be tuned. We analyze the band structure of these nanocrystals using optical absorption spectroscopy (OAS), a standard technique in use since the very beginning of semiconductor research. Natural ferritin contains a ferrihydrite core, often written as Fe(O)OH for convenience. Our selection of samples includes the Fe(O)OH core native to ferritin, various sizes of reconstituted Fe(O)OH cores, reconstituted

Fe(O)OH cores with anions co-deposited into the lattice during synthesis, and a variety of other transition metal oxides. The main result of this thesis is that selectively controlling each of these parameters allows us to tune the band gap from 1.60-2.38 eV.

This thesis is structured as follows: Chapter 1 contains the necessary background information to understand band gaps, the ferritin protein, and current solar energy technology. Next, Chapter 2 outlines the experimental methods used to create and characterize the nanocrystals. Band gap measurements for the wide variety of nanocrystals are presented in Chapter 3. The theory and methodology for calculating efficiency limits using these nanocrystals and the results of those calculations are included in Chapter 4. Finally, we end with conclusions and future directions for this work in Chapter 5.

1.2 Band Gaps

The band structure of solids describes the allowable states of their electrons, and thus optical absorption and emission properties through transitions between those states. However, unlike atoms and molecules, entire regions or "bands" of allowable energy states exist, so instead of distinct absorption lines there are continua of photon energies that can be absorbed. These bands arise from the periodic crystal lattice where the degeneracy of atomic orbitals causes splitting, forming continuous bands of allowable states from those orbitals.

The collection of bands, showing all the possible energy states at different momenta, is known as the band structure. The highest energy band with ground state electrons is called the valence band, while the lowest energy band with no ground state electrons is called the conduction band. The band gap is defined as the energy difference between the valence band maximum and conduction band minimum. If those two points overlap in momentum space, this is known as a direct band gap. A qualitative example of this is shown in Fig. 1.1(a). If they are offset in momentum

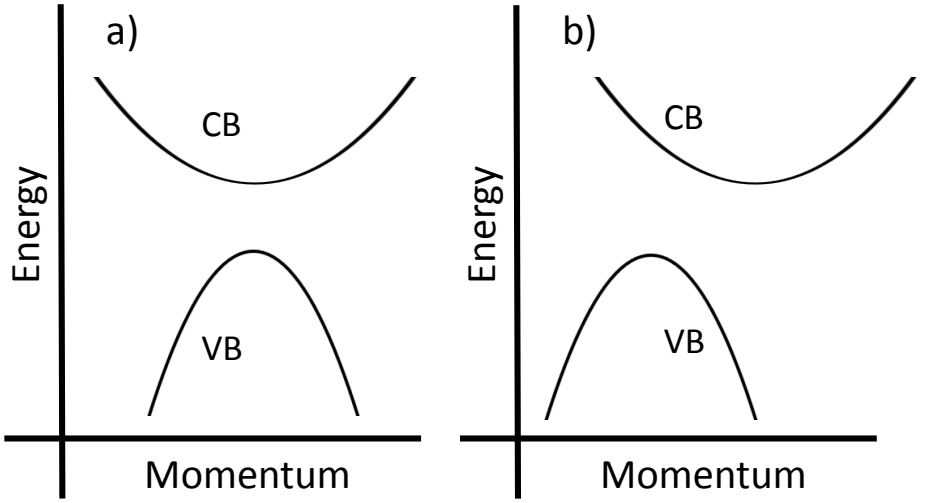

Figure 1.1 General band structure for (a) direct gaps and (b) indirect gaps. The upper curves show the conduction bands and the lower curves the valence bands.

space, this is known as an indirect band gap. A qualitative example of an indirect gap is depicted in Fig. 1.1(b).

Classifying a material as a metal, semiconductor, or insulator depends on the existence of a band gap, and size of that gap if it exists. A metal is a material where the valence and conduction bands overlap, leaving easily available states through which electrons can flow. Materials with a band gap are either semiconductors or insulators, depending on the size of the band gap. Semiconductors typically have band gaps up to about 3 eV, and insulators band gaps beyond that.

Optical transitions are possible in semiconductors, allowing for many useful applications. Their band gaps often correspond to energies in the visible spectrum. This has allowed for technologies like light emitting diodes (LEDs). Besides emitting light in visible frequencies, semiconductors can also be used to absorb light and convert it to electricity. Given that roughly 43% of the solar energy that reaches Earth's surface is visible [1], semiconductors have ideal band gaps for this task.

Absorption can happen from one of two types of optical transitions in semiconductors, direct

and indirect. Direct transitions require no appreciable change in momentum for the electron, so only a photon of sufficient energy is needed to excite the transition. For indirect transitions, a significant change in momentum is required [2]. Since photons carry negligible momentum compared to electrons, they cannot provide the necessary momentum to induce the transition on their own. Instead, a sufficiently energetic photon provides the change in energy, while the absorption or emission of a phonon (lattice vibration) provides the necessary change in momentum. Because this is a two step process, it is much less probable than a direct transition. A semiconductor is classified as direct or indirect depending on type of transition across the band gap. Note that while the lowest energy transitions across the band gap of an indirect gap semiconductor are indirect transitions, it is still possible to have direct transitions at higher energies. The onset of these transitions is sometimes called the direct gap, as will be done in this thesis, even though it is not the true band gap of the material [3].

Different techniques can be used to measure band gaps depending on the type of band gap, be it direct or indirect. Photoluminescence (PL) is often the simplest method, where high intensity light well above the band gap is used to excite electrons, then the emitted PL is analyzed by a spectrometer. The emission peak is identified as the band gap. Indirect gap materials have very weak PL due to the lower probability of transitions, therefore PL typically cannot be used to measure the band gap for these materials. Instead of monitoring the emission of the sample, one must monitor the absorption. The wavelength dependence of that absorption yields the band gap after some mathematical analysis. Details of this process are outlined in Section 2.2.

1.3 Ferritin Protein

Ferritin is a 12 nm diameter spherical protein used for iron storage in most complex organisms that can also serve as a template for diverse nanocrystal synthesis. It encloses an 8 nm diameter

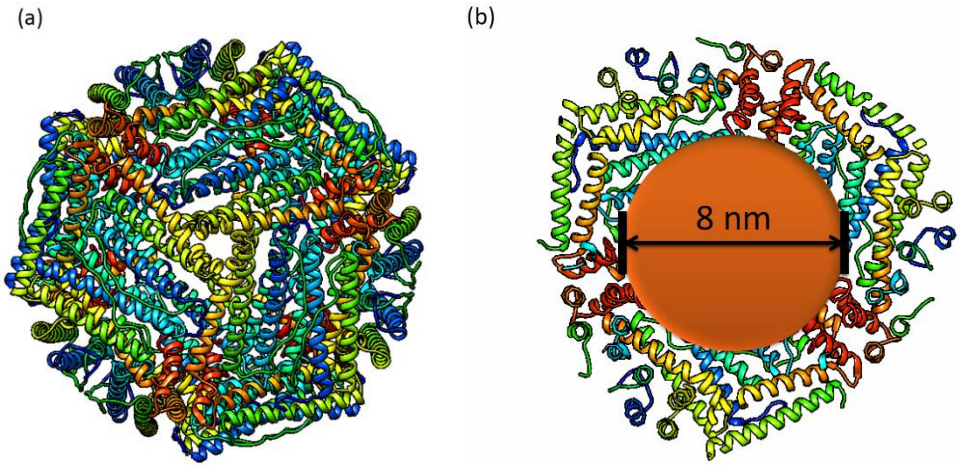

Figure 1.2 (a) Ferritin structure showing the different subunits. (b) Cross section showing the mineral core and channels through the shell.

cavity with a number of channels that allow molecules to pass in and out of the protein, as can be seen in the center of Fig. 1.2(a) or along the edges of Fig. 1.2(b). Naturally it contains a ferrihydrite nanocrystal core. Ferritin with its natural core is known as native ferritin. Through certain chemical processes that nanocrystal can be deconstructed and removed, yielding an empty protein shell called apoferritin [4]. A wide variety of metal oxide and II-VI semiconductors can then be synthesized within apoferritin; however, accurate characterization of their band gaps is missing [5–14].

Two types of sub-units make up the ferritin protein—heavy and light chain—and each serve a different purpose. A total of 24 sub-units come together to form one ferritin molecule. They serve different purposes and total 24 for each ferritin molecule. Light chain sub-units contain nucleation sites for core mineralization [15] and facilitate electron transfer across the protein shell [16]. Heavy chain sub-units contain the ferroxidase center which oxidizes loose metal ions in solution, reattaching them to the nanocrystal [17, 18].

A number of important properties must be met for ferritin to successfully harvest solar energy.

First, it must be possible to extract excited electrons from the protein shell. Ferritin was proven conductive through conductive atomic force microscopy [19], and as discussed above that conduction takes place across the light chain subunit [16]. Also, excited electrons have been used to reduce gold chloride in solution to form gold nanoparticles on the outer surface of ferritin [20]. This shows that electrons can be extracted from inside the ferritin to do meaningful electrical work. Second, it must be possible to attach ferritin to an electrode. This also has already been proven [21, 22]. Finally, nanocrystals within ferritin must have suitable band gaps to absorb significant portions of the solar spectrum, while doing so with high efficiency. Demonstrating that will be the main focus of this thesis.

In addition to the field of solar energy, ferritin offers interesting applications in nano-engineering. It can be deposited in controlled arrays on a substrate [23] and manipulated by attaching DNA strands to the surface [24]. Once deposited in an interesting configuration, the protein can be baked off and the remaining Fe(O)OH nanocrystal used as a catalyst for carbon nanotube growth [17]. None of this is specifically examined in this thesis, but these features open up interesting future applications for ferritin.

1.4 Previous Band Gap Measurements of Nanocrystals in Ferritin

Multiple studies have reported the band gap of native ferritin and its naturally occurring Fe(O)OH core with small amounts of phosphate, though they contradict each other and range anywhere from 1.0 to 3.5 eV [20, 25, 26]. Furthermore, none of these studies utilized the standard optical techniques of photoluminescence and optical absorption that have been in use for decades [27], instead opting for less direct means of measuring the band gap.

The first reported value for the band gap of native ferritin was 2.5-3.5 eV, found using selective

light filters while monitoring a photochemical process [25]. Later on a narrower range of 3.0-3.35 eV was given, again using selective light filters while monitoring a different photochemical reaction [20]. Neither of these studies was able to identify the band gap as indirect or direct.

Several groups have also used scanning tunneling spectroscopy (STS) to measure the band gap of native ferritin. This involves positioning the tip of a scanning tunneling microscope (STM) at a fixed location and scanning the voltage between the tip and base, measuring the current at each voltage. In theory, the voltage where the current starts increasing rapidly corresponds to the band gap. Liu et al. reported a band gap of 1.5 eV for 500 Fe atoms per ferritin and 2.7 eV for 2000 Fe atoms per ferritin, a trend opposite what would be expected from quantum confinement where constraining the electron to smaller volumes increases band gap energies [28]. Presinger et al. also used STS on the chemically similar hematite (Fe_2O_3), reporting a value of 1.8-2.2 eV with a 1.3 eV surface state [29]. Finally, Rakshit et al. presented a band gap of 1.0 eV for native ferritin using STS [26]. There are known issues with using STS to measure nanocrystal band gaps [30]. For example, it is most sensitive to surface states, not the true band gap of the material, and is unable to characterize the type of band gap.

Ferrihydrite is only one of many mineral forms of iron oxide. It is most similar in chemical composition to hematite (Fe_2O_3), so it is expected to have a similar band gap. Hematite nanocrystals were found to have an indirect band gap of 2.2 eV, an impurity defect state at 1.8 eV [31], and a direct transition at 3.1 eV [32]. Given the similarity, measured band gaps for Fe(O)OH nanocrstals should be close to these.

Certain non-native metal-oxides have also been studied in ferritin. Rakshit et al. also performed STS measurements on cobalt and manganese oxyhydroxide [Co(O)OH and Mn(O)OH] nanocrystals. They reported band gaps of 0.90 eV for Co(O)OH and 1.17 eV for Mn(O)OH [26]. However, given the failure of this method to accurately establish the band gap for native ferritin, as will be shown in Chapter 3, additional investigation of these materials was warranted. We also

investigate titanium oxyhydroxide nanocrystals, often written as Ti(O)OH, for which there have been no band gap measurements reported . Similarly the chemical synthesis of Fe(O)OH codeposited with anions into ferritin is well established, but the characterization of the anions' impact on the band gap is missing [33].

1.5 Photovoltaic Cells

The goal of this thesis is to characterize nanocrystals encapsulated by ferritin for potential photovoltaic applications. Traditional photovoltaic cells use a p-n junction to separate electrons from holes and create a photo-induced current. The band gap of the semiconductor used dictates which wavelengths of light are absorbed. Photons with energy below the band gap will pass through, while photons with energy equal to or above the band gap are absorbed. For a given amount of illumination, the I-V characteristic curve (more detail in Section 4.1) describes the relationship between current and voltage. An example is provided in Fig. 1.3. Electrical power is then maximized by tuning the resistance of the load, and thus the voltage drop across it. Current varies minimally until the recombination current becomes significant, an effect which arises from electrons and holes recombining before they can be swept out of the diode structure. The open circuit voltage ($I = 0$) is the point where the recombination current equals the photo-induced current. Naturally, there will be a maximum electrical power somewhere between zero voltage and the open circuit voltage, e.g. approximately 1.7 V in Fig.1.3.

1.5.1 Shockley-Queisser Limit on Photovoltaic Efficiency

While photons with energy greater than the band gap are readily absorbed, the excited electrons rapidly relax to the conduction band minimum, releasing their excess energy as heat in the form of phonons. Thus, when selecting a semiconductor with a suitable band gap for efficient solar

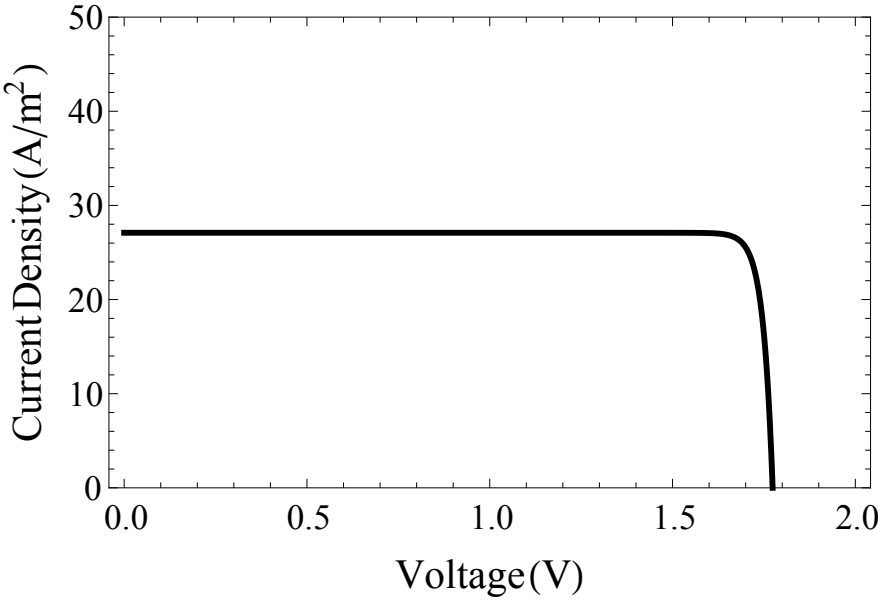

Figure 1.3 An example of an I-V characteristic curve. Due to the coupling between current and voltage, there is a trade-off that results in a unique optimal operating voltage to maximize electrical power.

energy conversion, a natural trade off exists. Too low of a band gap results in large losses to heat. Too large of a band gap and too many photons with energy below the band gap go unabsorbed. This trade off results in a maximum possible efficiency for any individual solar of 33.7%, known as the Shockley-Queisser limit [34]. The theory of this limit is outlined in Section 4.1.

Efficiencies beyond Shockley-Queisser limit can be achieved with multi-junction solar cells, where several different materials with a range of band gaps are used. Layering solar cells allows for the higher energy photons to be absorbed first with less loss to heat. The lower energy photons that pass through then impact the next layer. Concentrating the sunlight also brings increased efficiency. Allowing for multi-junction solar cells and concentrated sunlight raises the theoretical efficiency limits to 40%, 55%, and 63% for one, two, and three layer solar cells with the right band gaps [35]. As the number of layers approaches infinity, the maximum efficiency approaches 86% [35]. Such high efficiencies are more than just theoretical, actual multi-junction devices have

surpassed 40% efficiency [36].

1.5.2 Nanostructured Photovoltaics

In addition to multi-junction solar cells, nanostructured solar cells offer a number of advantages over their bulk counterparts. Quantum dot solar cells as shown in Fig. 1.4 are modeled on dye-sensitized solar cells, where the light absorbers (dye molecules or quantum dots) are attached to TiO_2 nanoparticles on an electrode [37,38]. Excited electrons are channeled to the electrode and then continue to power the circuit. They return to the counter electrode, which is separated from the light absorber by an electrolyte solution capable of cycling the electrons back to the ferritin, thus closing the circuit.

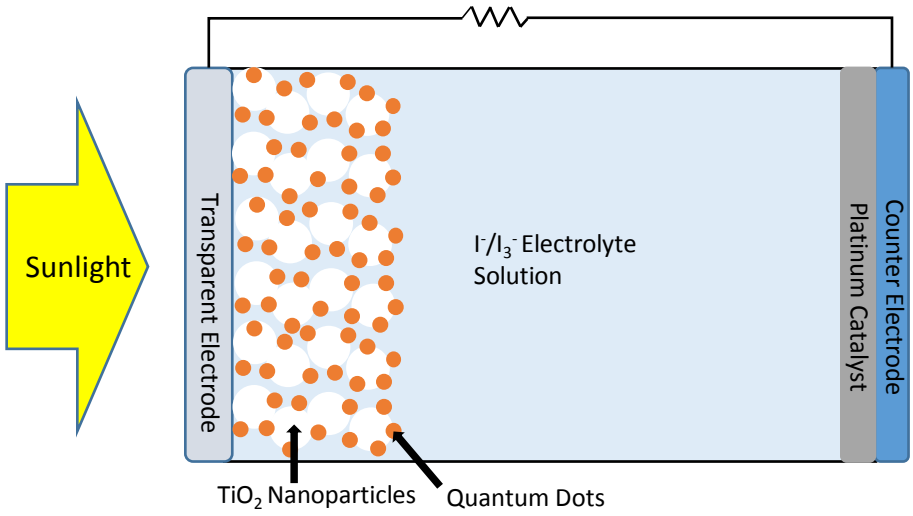

Figure 1.4 A typical quantum dot solar cell. Excited electrons from the quantum dots flow to the TiO_2 nanoparticles, power a load, and then return through the counter electrode. The electrolyte solution returns electrons to the quantum dots through a redox reaction that is catalyzed by the platinum layer.

Several properties make nanostructured photovoltaics attractive candidates for harvesting solar energy. Quantum dot band gaps are tunable through quantum confinement, where energy levels

rise as the particle size approaches the Bohr radius of photo-excited electrons [39]. This gives greater control to select the optimum band gaps for the greatest efficiencies in single and multi-junction solar cells. Furthermore, multiple excitation generation has been shown to be much more likely in quantum dots than in bulk semiconductors [40], giving additional increases to maximum efficiencies [41]. This results from photons with energy of at least twice the band gap exciting multiple electrons, thus losing less energy to heat. Up to seven excitons have been generated from a single photon in PbS quantum dots [42], and the additional electrons from such events have been electrically extracted [43]. Multi-junction quantum dots solar cells have already been constructed and convert sunlight with greater efficiency than any of the layers on their own [44].

Ferritin nanocrystals offer additional advantages beyond those provided by typical quantum dots. The protein shell serves to protect the nanocrystals and prevent conglomeration in solution. It can also be used to control the nanocrystal arrangement on a substrate. The ferroxidase center heals the effects of photo-corrosion by capturing, reoxidizing, and reattaching loose atoms that have been photo-reduced [18]. This makes it an ideal candidate for use in nanostructured photovoltaics.

Chapter 2

Experimental Methods

This chapter outlines the experimental methods used in measuring band gaps and describes the general synthesis method used to form the types of nanocrystals studied. We outline the experimental setup and data analysis, then discuss pitfalls to look for in the process.

2.1 Nanocrystal Synthesis

All sample preparation was performed by Dr. Richard Watt's lab of the BYU Chemistry Department. Since I was not specifically involved in the synthesis, only a brief description is included here. Apoferritin is prepared by removing the native Fe(O)OH core from ferritin through iron chelation, where certain reagents pass through the channels and are used to strip the nanocrystal of individual iron atoms [45]. Nanocrystal synthesis methods vary, but in general ions enter ferritin through its channels and react with oxygen in the interior to form the nanocrystal, often assisted by the ferroxidase center. References to the relevant literature outlining the different synthesis method used in this study will be provided at the beginning of the relevant sections of Chapter 3 where the resulting samples are discussed.

Core sizes are represented by a metal atom/ferritin ratio. They were measured through a com-

bination of inductively coupled plasma mass spectrometry (ICP-MS) and protein content analysis of a test solution. The total number of metal atoms in the test solution is determined by ICP-MS and the total number of ferritin molecules by the Lowry method [46]. The ratio of the two results yields metal atoms per ferritin, a measure of the nanocrystal size.

2.2 Optical absorption spectroscopy

Band gaps are measured with optical absorption spectroscopy (OAS), using the wavelength dependence of absorption to calculate the band gap. A schematic of the experimental setup is shown in Fig. 2.1. Monochromatic light is obtained from an Oriel 66011 xenon arc lamp sent through a Digikrom 250 spectrometer. This light is then modulated with a mechanical chopper and focused through the sample solution into a photodiode detector. To reduce noise, experiments are performed in the dark with the photodiode signal sent to a lock-in amplifier referenced to the chopper [30]. A computer reads the lock-in signal while stepping through spectrometer wavelengths.

For typical experiments the resolution the spectrometer was 1.6 nm, obtained from 0.5 mm openings on the entrance and exit slits. We used two different wavelength ranges, one for measuring indirect gaps and one for measuring higher energy direct gaps. The separate ranges were selected based on the wavelength responses of the available spectrometer gratings. Wavelength ranges typically cover 350-810 nm for indirect gaps and 250-500 nm for direct gaps. A cutoff of 810 nm was chosen because it is sufficiently far below the band gap of all the materials studied, while avoiding the first sharp spectral line from the Xe lamp. If desired, ranges for indirect gaps can be extended to approximately 1300 nm, but the large spectral lines from the Xe lamp beyond 810 nm can interfere with the signal. Signals in a lock-in amplifier linger, decaying by 1/e over the duration of one time constant. If long wavelengths above 810 nm are desired, longer dwell times between data points are needed to ensure that no residual signal from the lamp's spectral

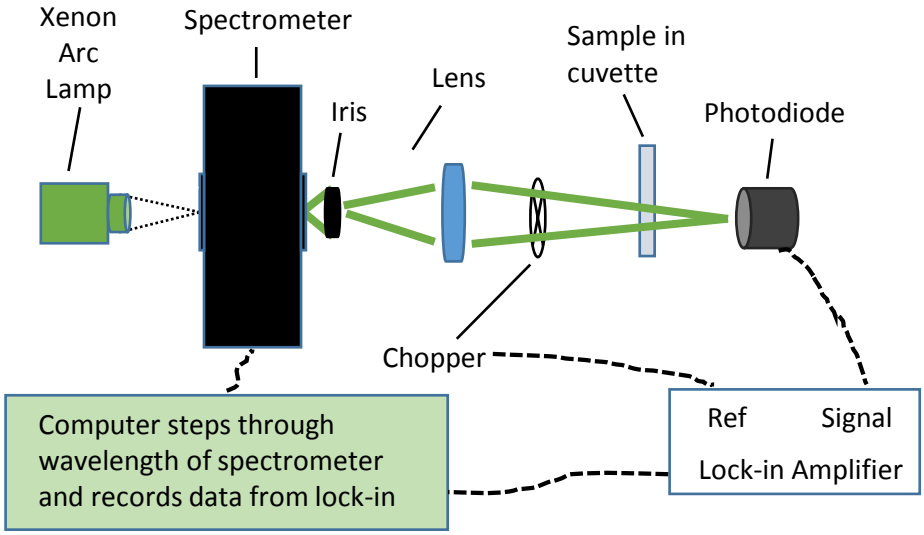

Figure 2.1 Schematic of optical absorption experiment. Broad spectrum light from a xenon arc lamp is sent through a spectrometer to select individual wavelengths. The monochromatic light gets modulated by a mechanical chopper then focused through the sample in solution and into a photodiode detector. The photodiode signal is analyzed through a lock-in amplifier referenced to the chopper while a computer steps through spectrometer wavelengths.

lines remain in the lock-in for the next wavelength. Without this precaution, at wavelengths near the spectral lines of the Xe lamp it will appear as though there is much more light incident on the sample than the lamp actually produces. Typically, dwell times of five times the lock-in time constant are sufficient. Staying below 810 nm allows for shorter integration times of three times the time constant since the signal does not vary greatly from point to point.

2.2.1 Raw Data

Absorption data is obtained by comparing two wavelength scans. First, a blank sample that is an identical solution except without any ferritin is placed in the cuvette and the transmitted power is measured over a range of wavelengths. Next, the transmitted power through the cuvette with the ferritin sample is measured over the same range of wavelengths. The ratio of the two then gives

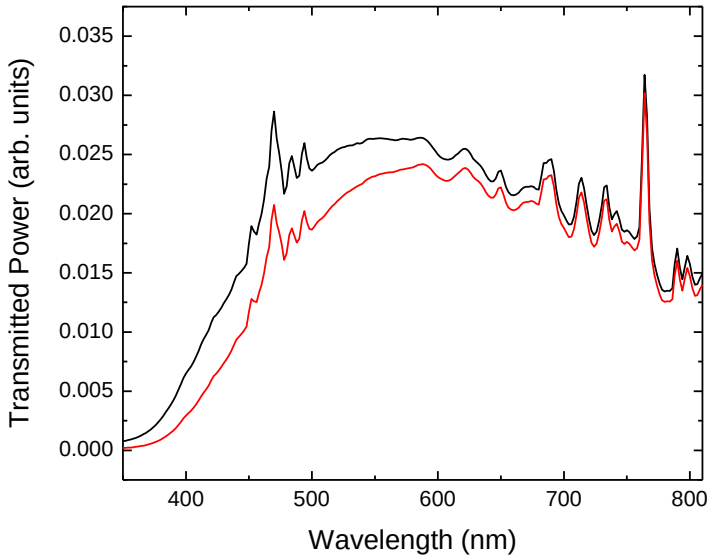

Figure 2.2 Representative raw spectra of ferritin and blank solutions. The ferritin solution is shown in red and the blank solution (identical except without ferritin) is shown in black. The difference between the two is the light absorbed by the sample.

the fraction transmitted (and thus also the absorption) at a range of wavelengths. Representative raw data is shown in Fig. 2.2. Observe that the absorption dies off at longer wavelengths/lower energies, which is indicative of a band gap somewhere in the vicinity.

There are a number of requirements for high quality data. If the absorption is too weak, the signal to noise ratio suffers. On the contrary, if the absorption is so strong that it quenches all of the light at a number of wavelengths, it is impossible to determine the wavelength dependence of absorption over those wavelengths, hence the band gap cannot be extrapolated. The overall absorption can be tailored by changing the concentration of ferritin in the solution. A good amount of absorption is shown by the raw data in Fig. 2.2. Depending on the exact mineral inside of ferritin, roughly 0.1-0.2 mg/ml serves as a good starting point.

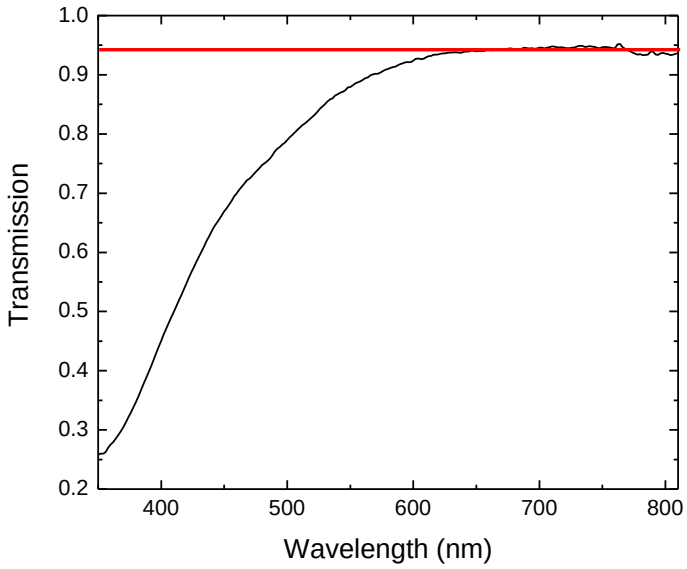

Figure 2.3 Transmission curve for the data displayed in Figure 2.2, obtained by dividing the ferritin scan by the blank. Note the leveling off below 100% transmission, indicating that loss to scattering must be accounted for.

2.2.2 Normalizing Transmission

Depending on the sample, up to about 10% of the incident light can be lost to scattering. This compromises the data because it would appear that light with energy below the band gap is being absorbed. Consequently, this pushes the extrapolated band gap below its true value. This loss is uniform across all wavelengths, so the data may be normalized to account for it. To do this, we simply divide the raw transmission by the value it levels off at (e.g., divide the data in Fig. 2.3 by approximately 0.94). This corrects for the loss to scattering and results in the transmission actually reaching 100% for energies below the band gap.

2.2.3 Data Analysis

The absorption coefficient α of a material is given by

$$I_t = I_i \exp(-\alpha z), \tag{2.1}$$

where I_i is the incident intensity, I_t is the transmitted intensity, and z is the thickness of the material. Thus, by rearranging the preceding expression, absorption coefficients are calculated point-by-point using the intensity transmitted through the blank and ferritin samples for I_i and I_t, respectively

$$\alpha \propto -\ln\left(\frac{I_{ferritin}}{I_{blank}}\right). \tag{2.2}$$

The actual value for z turns out to be irrelevant; the relationship between α and photon energy determines the band gap independent of constant multiples. Thus when solving for α, one may simply assume arbitrary units where $z = 1$. With certain reasonable approximations, such as negligible exciton effects and an allowed band gap transition, the relationship between α and photon energy is given for direct gaps by [27]

$$\alpha \propto \left(E_{photon} - E_{gap}\right)^{1/2}, \tag{2.3}$$

for indirect gaps where a phonon is absorbed by

$$\alpha \propto \left(E_{photon} - E_{phonon} - E_{gap}\right)^{2}, \tag{2.4}$$

and for indirect gaps where a phonon is emitted by

$$\alpha \propto \left(E_{photon} + E_{phonon} - E_{gap}\right)^{2}. \tag{2.5}$$

These equations are valid where $E_{photon} \geq E_{gap}$ for direct gaps and where $E_{photon} \geq E_{gap} \pm E_{phonon}$ for indirect gaps where a phonon is emitted or absorbed. Typically both Eq. 2.4 and Eq. 2.5 are allowed for indirect gaps, but the relative probabilities of the two depend on the temperature of the material.

From Eqs. 2.3-2.5, α is proportional to either photon energy squared or square rooted. It follows that α^2 (for direct gaps) and $\sqrt{\alpha}$ (for indirect gaps) are linear functions of photon energy. Because of this linear relationship, linear fits are made and then extrapolated to the x-axis to yield the band gap (plus or minus phonon energy for indirect gaps). See Fig. 2.4 for examples of both

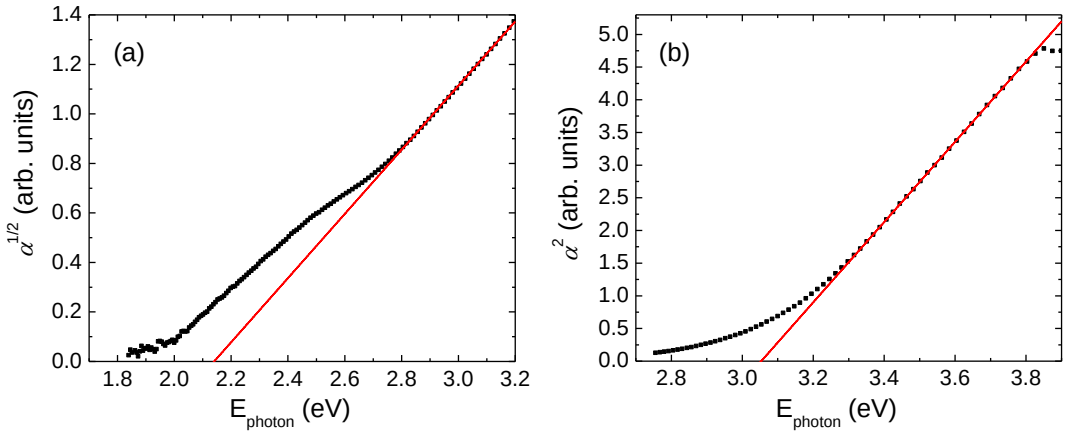

Figure 2.4 Linear extrapolations of the (a) indirect gap and (b) direct gap of native ferritin. The x-intercept of the linear fit yields the band gap (Eqns. 2.3-2.5), in this case 2.14 eV for the indirect plot and 3.05 eV for the direct plot. Note the lower energy indirect feature which we attribute to a defect state. Details of this analysis are found in Section 3.1. This figure is reproduced from [30].

types of transitions. Because of the judgment call needed for the bounds of the fit, there is inherent uncertainty in band gap measurement due to those bounds.

In the ferritin samples studied, we did not observe two distinct transitions, meaning one of two things: the phonon energy is too small to distinguish, or so large that at room temperature very few phonons of sufficient energy can be found, suppressing the phonon absorbing transition. For the latter, the x-intercept is actually the value of the band gap plus phonon energy, but for simplicity we refer to it as simply the band gap. Regardless, it is the energy where significant absorption begins, which is the interesting value for applications in solar energy.

Chapter 3

Band Gap Results

In this chapter we outline the resulting band gaps for the various types of nanocrystals. We begin with an apoferritin control so that we can be certain that any features we see are due to the encapsulated nanocrystals, not the protein itself. Next, we resolve discrepancy from the literature about the band gap of native ferritin. We investigate the change in band gap with time from different synthesis techniques, followed by experiments on how the band gap of reconstituted ferrihydrite can be tuned by co-depositing anions during nanocrystal synthesis. Finally, other types of metal-oxide not naturally found in ferritin are presented, as well as a new synthesis method for making mixed cores of two different transition metals.

3.1 Apoferritin and Native Ferritin

To measure the band gaps of the encapsulated nanocrystals, one must first account for the absorption of apoferritin. The protein was found transparent to all light below 4.0 eV where direct absorption begins, as seen in Fig. 3.1.

As described in Chapter 1, there was previous disagreement in the literature concerning the band gap of native ferritin. Using OAS, we found native ferritin to be an indirect gap semiconductor

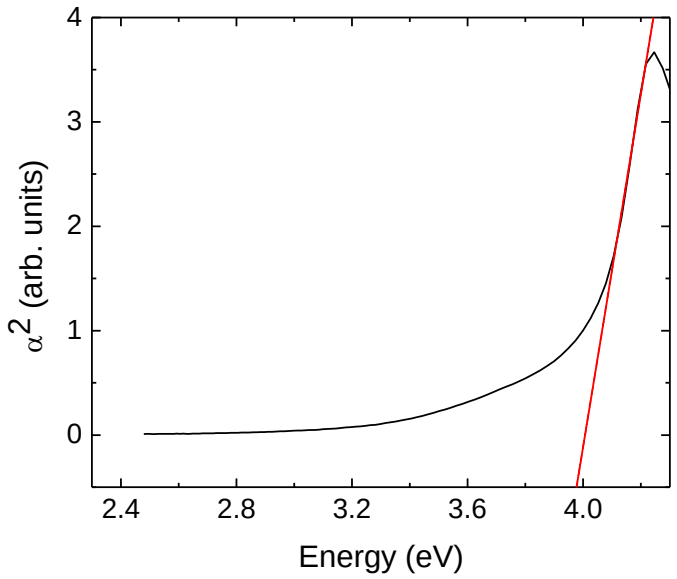

Figure 3.1 Direct absorption of apoferritin, showing an absorption edge at 4.0 eV.

with a band gap of 2.14 eV and a direct gap of 3.05 eV. The data and fits used to arrive at these values were shown in Fig. 2.4. In addition to the indirect band gap, a defect state is found at 1.92 eV. Having a band gap close to that of hematite, a similar mineral phase of iron oxide, supports the validity of these measurements. Ferrihydrite's indirect band gap of 2.14 eV falls near hematite's 2.2 eV indirect band gap [32]. Similarly, the 3.05 eV direct gap and 1.92 eV defect state of ferrihydrite line up with the 3.1 eV and 1.8 eV direct gap and defect state of hematite [31, 32].

Much of the discrepancy in the previous literature can be resolved by taking into account the type of transition and the methods used by those groups. The groups using selective optical filters to monitor photochemical processes will naturally be biased to direct transitions given their much greater impact on absorption. Reported ranges of 2.5-3.5 eV [25] and 3.0-3.35 eV [20] both contain the direct gap of native ferritin as measured by us. On the other hand, STS is more sensitive to surface defects, so those studies reported much lower values [26, 28]. They reported values closer to the indirect band gap of the ferrihydrite in native ferriti as measured by us.

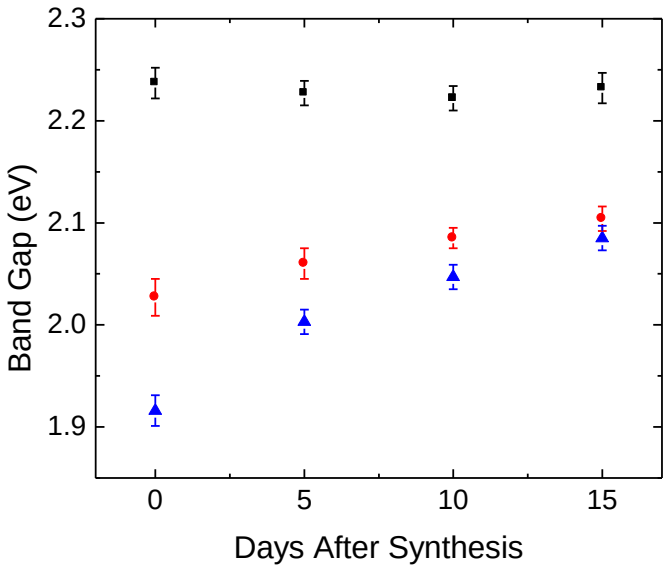

Figure 3.2 Indirect band gap aging of Fe(O)OH reconstituted in the TRIS buffer. Core sizes were 640, 980, and 1200 iron atoms/ferritin for black squares, red circles, and blue triangles respectively. After synthesis the cores crystallized with time, where the larger cores required more time to reach their final state.

3.2 Aging of Reconstituted Fe(O)OH

Depending on the pH buffer used during synthesis, Fe(O)OH crystallizes in one of two forms: 2-line and 6-line, so named for their diffraction spectra. Synthesis requires a stable pH, so it is performed in the presence of a pH buffer [47]. For 2-line Fe(O)OH, the proper pH is maintained by the buffer TRIS, while for 6-line the pH is maintained by the buffer imidazole. Band gaps were measured shortly after synthesis, and then repeated several times after five day intervals. Fig. 3.2 shows significant changes in the 2-line Fe(O)OH band gap, where the nanocrystals appeared to "age" and increase in band gap with time before leveling out to a steady state value. We theorize that after using the TRIS buffer, the ferritin core is still largely amorphous and only fully crystallizes over a period of about two weeks. Amorphous cores will have more defect related transitions, yielding lower measured band gaps. Furthermore, larger cores saw a larger change, likely due to having more opportunities for lower energy defects. With time, as the core crystallized the measured band

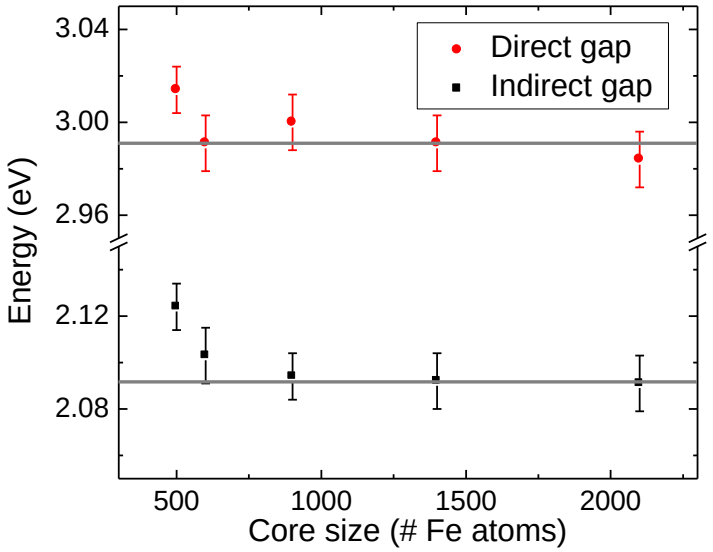

Figure 3.3 Size-dependent band gaps of reconstituted Fe(O)OH using the imidazole buffer. Gray lines show the "bulk-like" state where quantum confinement effects are no longer seen. Black squares show the indirect gaps and red circles the direct gaps. This figure is reproduced from [48].

gap increased.

Similar drawn out aging was not seen in the 6-line Fe(O)OH prepared with imidazole. Some change was observed within the first few hours after synthesis, but thereafter the samples had all already reached a steady state. Given the similarity between the final 2-line and 6-line band gaps, for most applications imidazole proves a more convenient synthesis buffer and was used in all the Fe(O)OH samples discussed below.

3.3 Tuning the Band Gap of Fe(O)OH by Co-Depositing Anions

During the synthesis of reconstituted Fe(O)OH, various anions (negative ions) can be co-deposited alongside the iron and incorporated into the mineral. Depending on the the amount

added, various anion to iron ratios can be achieved. Three different sets of samples were studied, following the synthesis methods outlined by Hilton [33], Polanams [10], and Smith [48]. One set was synthesized with co-deposited halides and more two where an assortment of oxo-anions were co-deposited in both 1 mM and 5 mM concentrations. This resulted in different degrees of co-deposition. A summary of the sizes of the samples, amounts of anion co-deposited, measured band gaps, and change in band gap relative to the anion-free bulk-like samples are provided in Table 3.1. Detailed discussion is provided in Subsections 3.3.1 and 3.3.2. For more in-depth analysis see our recently published paper [48].

With nanocrystals, quantum confinement can have a significant impact. Therefore, to properly attribute shifts in band gap to the codeposited nanocrystals, the nanocrystals must be sufficiently large to avoid quantum confinement effects. For reconstituted Fe(O)OH, we found that after reaching a size of 900 iron atoms per ferritin, the nanocrystals reached a bulk-like state where increases in size no longer corresponded to decreases in band gap. This can be seen with the leveling of the data in Fig. 3.3. All co-deposited samples were targeted to have sizes in this bulk-like regime.

3.3.1 Effect of Halides

In previous work, we showed that slight shifts in the band gap of native ferritin can be obtained by adsorbing halides (e.g. F^-, Cl^-, Br^-, and I^-) to the surface of the nanocrystal [30]. Incorporating them throughout the entire nanocrystal, not just the surface, was expected to result in even larger shifts in band gap. For each of the halides, ion-selective electrodes showed that approximately one halide was incorporated for each ten iron atoms. Similar to our work adsorbing halides to the surface, co-depositing them into the nanocrytal decreased the band gap, though this time in greater measure. Change relative to the bulk-like state is shown in Fig. 3.4. The indirect gap was lowered by as much as 0.058 eV with I^- and the direct gap by as much as 0.060 eV in the case of Br^-.

Anion	Iron/ ferritin	Anion/ ferritin	Indirect gap (eV)	ΔIndirect (eV)	Direct gap (eV)	ΔDirect (eV)
No salt - bulk	900±71	n/a	2.092±0.011	n/a	2.992±0.012	n/a
Halides						
F^-	2650±430	260	2.078±0.012	-0.014	2.991±0.008	-0.001
Cl^-	2090±280	210	2.077±0.012	-0.015	2.974±0.010	-0.018
Br^-	2400±250	240	2.032±0.012	-0.060	2.942±0.016	-0.050
I^-	2600±300	260	2.050±0.012	-0.042	2.934±0.014	-0.058
1 mM oxo-anions						
PO_4^{3-}	2000±400	185	2.139±0.010	0.047	3.009±0.008	0.017
MnO_4^{2-}	2000±300	75	2.080±0.010	-0.012	2.994±0.008	0.002
MoO_4^{2-}	1175±200	95	2.116±0.012	0.024	2.990±0.010	-0.002
WO_4^{2-}	1750±100	1000	2.215±0.012	0.123	3.058±0.008	0.066
5 mM oxo-anions						
PO_4^{3-}	430±53	60	2.380±0.024	0.288	3.231±0.014	0.239
MnO_4^{2-}	127±24	112	1.988±0.012	-0.104	2.878±0.010	-0.114
MoO_4^{2-}	1075±140	345	2.113±0.010	0.021	3.001±0.010	0.009
WO_4^{2-}	1060±120	1430	2.242±0.010	0.150	3.062±0.012	0.070

Table 3.1 Core sizes, type of anion, amount of anion co-deposited, measured band gaps, and change in band gap relative to the anion-free bulk-like state. This table is reproduced from [48].

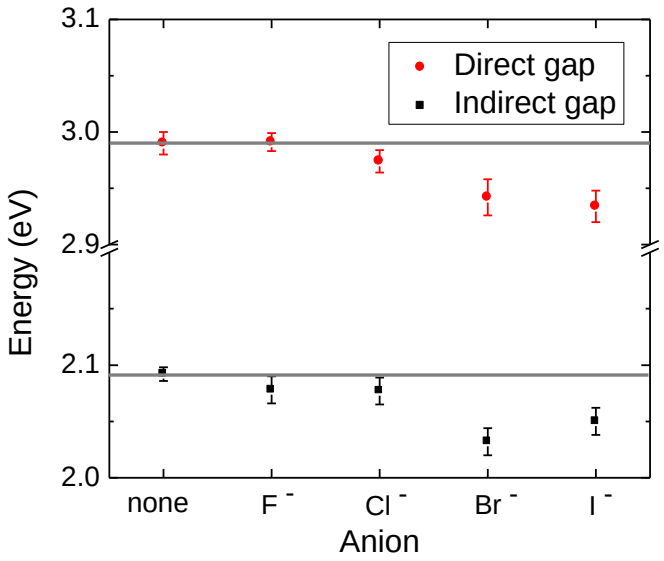

Figure 3.4 Changes in band gap due to co-deposited halides. Black squares show the indirect gaps and red circles the direct gaps. Solid gray lines show the values for the bulk-like state. Specific values are found in Table3.1. This figure is reproduced from [48].

3.3.2 Effect of Oxo-Anions

Using the co-deposition method of Polanams et al. [10], we successfully deposited the oxo-anions PO_4^{3-}, MnO_4^{2-}, MoO_4^{2-}, and WO_4^{2-} into the lattice. Details of the sizes of the nanocrystals and degrees of co-deposition are outlined in Table 3.1. Two different concentrations of oxo-anion where used during synthesis (1 mM and 5 mM) to target different iron to oxo-anion ratios. Throughout the remainder of this text the samples will be referred to by the oxo-anion and the concentration used during synthesis. As expected, the 5 mM samples showed greater levels of co-deposition.

The 1 mM PO_4^{3-} sample yielded 2000 iron atoms per ferritin with roughly 10% phosphate loading. This gave an indirect band gap of 2.139 eV and a direct gap of 3.009 eV (Fig. 3.5, Table 3.1). A large core size (>900 iron per ferritin) puts this sample in the bulk-like regime, so the

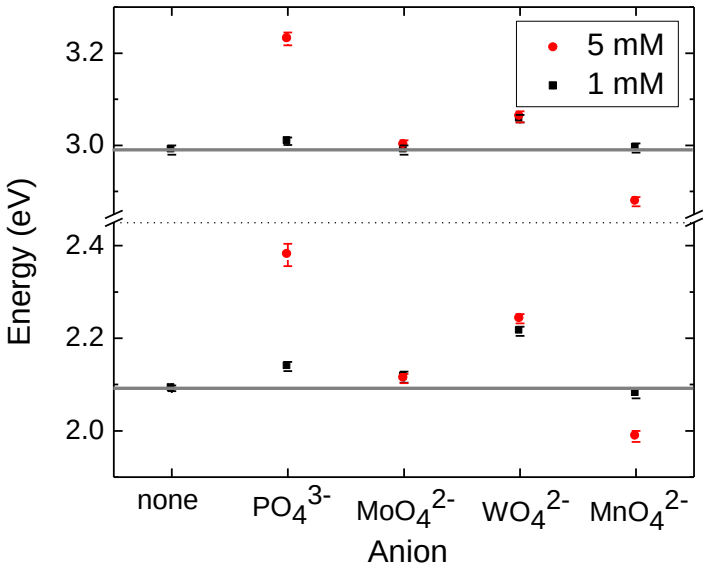

Figure 3.5 Changes in band gap due to co-deposited halides. Black squares correspond to 1 mM samples and red circles to 5 mM samples. The dotted line divides the region of plotted indirect gaps from the region of higher energy direct gaps. Solid gray lines show the values of the bulk-like state. Specific values are found in table3.1. This figure is reproduced from [48].

small variations from the bulk-like band gaps can be attributed to the co-deposited anions. It is interesting to note the similarity between this sample and native ferritin, which naturally contains about 10% phosphate. As discussed previously in section 3.1, native ferritin has an indirect band gap of 2.14 eV and a direct band gap of 3.05 eV.

Phosphate is known to inhibit iron from loading into ferritin [33], so as expected the 5 mM phosphate sample resulted in a much smaller nanocrystal of 430 iron per ferritin (Table 3.1). The resulting indirect gap was 2.380 eV, 0.288 eV higher than the bulk-like state. However, the size was too small to put it into the bulk regime. If we instead compare it to the 500 iron/ferritin anion-free sample, which had a shift of only 0.032 eV relative to the bulk-like state, we deduce that the majority of this change (roughly 0.256 eV) was due to the co-deposited anion.

Molybdate had no discernible impact on the band gap (Fig. 3.5, Table 3.1). The two different concentrations gave 6% and 30% anion loading and where in the bulk-like state, but neither

showed significant change in the band gap. This suggests no additional benefit from co-depositing molybdate into ferritin for absorption applications.

Co-depositing tungstate resulted in incredibly high levels of oxo-anion loading, with tungsten to iron ratios greater than one for the 5 mM sample (Table 3.1). This suggests that a new type of mixed mineral may have been formed. Both samples were large enough to be in the bulk-like state, so changes in band gap can be attributed to the co-deposited anions. Significant shifts in band gap are shown in Fig. 3.5. The 1 mM sample showed increase of 0.123 eV and 0.066 eV for the indirect and direct band gaps, while the 5 mM sample showed increases of 0.150 eV and 0.070 eV for the indirect and direct band gaps (Fig. 3.5, Table 3.1).

With the permanganate samples, the 5 mM sample saw significant shifts in band gap, while the 1 mM did not. 1 mM permanganate only resulted in 8% loading, giving no significant shift in band gap. On the contrary, the 5 mM sample resulted in roughly one to one permanganate to iron loading, but much smaller nanocrystals of 127 iron per ferritin. Given that permanganate is a strong oxidizing agent, it is possible that it replaced the role of oxygen during synthesis, resulting in a new mixed mineral core. The 5mM sample had an indirect band gap decreased by 0.104 eV and a direct gap reduced by 0.114 eV (Fig. 3.5 and Table 3.1). It was much smaller than the bulk-like state, so quantum confinement effects would cause an increase in band gap. Hence it is possible that the co-deposited anions had an even stronger effect that is being partially masked by quantum confinement. Furthermore, given that the band gap for Mn(O)OH nanocrystals in ferritin (Section 3.4) is lower than Fe(O)OH, we would expect this this mixed mineral core to have a lower band gap. This provides evidence for a mixed mineral core, which will be examined in greater detail in Section 3.5.

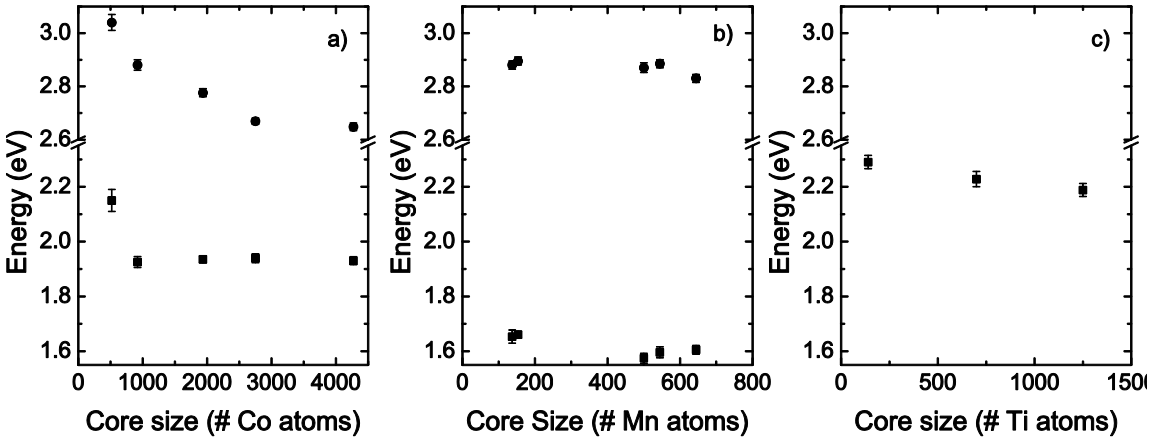

Figure 3.6 Band gaps for (a) Co(O)OH, (b) Mn(O)OH, and (c) Ti(O)OH nanocrystals in ferritin plotted against core size. Squares show indirect gaps and circles direct gaps. This figure is reproduced froms [49].

3.4 Non-native Metal-Oxides in Ferritin

Co(O)OH samples were prepared following the method outlined by Douglas et al. [5]. They were found to be indirect gap semiconductors with higher energy direct transitions. A wide range of core sizes were obtained, ranging from 500 to 4300, dislaying the effects of quantum confinement, and are plotted in Fig. 3.6(a). Larger core sizes reached a steady state with a band gap of 1.93 eV, while smaller cores reached as high as 2.15 eV. Direct gaps saw a larger trend of roughly 2.65-3.05 eV, depending on the core size. We should note the disagreement with the 0.90 eV value measured through STS [26]. Given the limitations of that method described in Section 1.4, we take our value to be more accurate and relevant, particularly when it comes to applications in solar energy. Measurements which monitor the absorption of light will naturally be more relevant to applications which depend on that same process.

Mn(O)OH samples were synthesized with the process developed by Meldrum et al. [8]. Once

again, a range of core sizes was targeted, but the actual sizes resulted in two clusters of similar size. Fig. 3.6(b) shows the band gaps of these samples, with band gaps of 1.60 eV and 1.65 eV for the larger and smaller sized nanocrystals, respectively. They also exhibited direct gaps of approximately 2.85 eV and 2.90 eV, respectively. These values expand the spectrum covered by all previously discussed samples, a necessary step in developing the diverse library of materials needed for harvesting solar energy. As before with Co(O)OH, a previous measurement of 1.17 eV was reported by Rakshit et al. [26], though for the same reasons we take our measurement to be the more accurate and relevant value.

Ti(O)OH nanocrystals were synthesized following the methods of Klem et al. [6]. A range of core sizes was obtained, resulting in a tunable band gap range from 2.19-2.29 eV as seen in Fig. 3.6(c). Due to proximity to the absorption edge of apoferritin at 4 eV and inability to decouple the two sources of absorption near 4 eV, no precise value for the direct gap is reported, though it appears to be approximately 3.8 eV.

3.5 New Manganese Oxide Synthesis

We have also been investigating a new class of manganese oxide synthesis, in which manganese ions undergo a comproportionation reaction with permanganate ions. Comproportionation is where the oxidation state of each precursor is oxidized or reduced to meet in the middle and form a new mineral. These samples had an indirect band gap of 1.95 eV, a direct gap of 2.74, and synthesis was most successful at 9.4 pH. This method can likely by extended to mixed metal cores, where metals transition metals like iron, cobalt, and nickel react with permanganate. Similarly, chromate may possibly serve as the oxidizing agent, yielding mixed cores of chromium with other transition metals.

3.6 Summary

Controlling the size and chemical composition of the nanocrystals, be it through different types of metal oxyhydroxides or co-depositing anions, allows us to tune the band gap of ferritin encapsulated nanocrystals over a range of 1.60-2.38 eV. This gives potential for interesting applications in solar energy. Maximum solar energy conversion efficiencies are presented in the next chapter to highlight that potential.

Chapter 4

Efficiency Theory

In this chapter we outline multi-junction solar cell efficiency theory, including cases for current matched multi-junction systems. We then present calculated efficiencies for various configurations that utilize the different ferritin materials discussed in Chapter 3. These efficiencies are represented graphically with their accompanying I-V characteristic curves and the voltages at which the layers must operate to optimize efficiency.

4.1 Calculating Maximum Theoretical Efficiencies

Efficiency theory for solar cells was first laid out by Shockley and Queisser [34], finding the maximum possible efficiency for a single junction solar cell to be 33.7%. This maximum is referred to as the Shockley-Queisser limit (see Section 1.5.1). We generally follow the method of Shockley and Queisser and the later extension by De Vos [35] for multi-junction solar cells, though with slight modifications [49]. Rather than model the solar irradience as a 6000 K blackbody, we use the actual average solar spectrum at the earth's surface (AM1.5G [50]). We also expand the calculations to a current matched multi-junction solar cell and utilize a more accurate value for the solid angle covered by the sun. We begin with calculations for parallel circuit multi-junction solar

cells, then describe necessary modifications for a current-matched system.

The total current I of a solar cell is the current induced by absorbed photons minus the recombination of electrons and holes. For the sake of these calculations, we assume negligible non-radiative recombination. Thus the total current is

$$I = I_{photon} - I_{recomb}. \tag{4.1}$$

The photon current arises from solar irradiance where we assume that each photon with energy greater than the band gap is absorbed and produces exactly one excited electon-hole pair (i.e. we ignore multiple exciton generation and assume sufficient material thickness that all photons that can be are absorbed). Photons with energy below the band gap pass right through. For a single junction device, an I-V curve is similar to Fig. 1.3. Maximizing the power $P = IV$ by finding where $\mathrm{d}P/\mathrm{d}V = 0$ yields the conditions for maximum efficiency. For multi-junction solar cells, mutual irradiance between neighboring layers induces coupling between them, yielding a system of non-linear transcendental equations that must be optimized.

First we define the recombination current, then the photon current. Recombination is when electrons and holes recombine before being shuffled away from the solar cell to power a circuit. In the dark, the number of electrons lost per unit time to radiative recombination must equal the number excited by the blackbody radiation of its surroundings. For the ith layer this is given by

$$F_{darkrecomb,i} = 2A \int_{E_{g,i}/h}^{\infty} N(f,T)\,\mathrm{d}f, \tag{4.2}$$

where A is the area of the cell and $E_{g,i}$ is the band gap of the ith layer. The factor of two arises from considering both the top and bottom surfaces of the cell. $N(f,T))$ is a modified version of the standard blackbody radiation formula, where we divide by hf to convert watts to photons per second and account for the solid angle incident on a planar surface, which adds a factor of π. This black body spectrum, in units of photons s^{-1} m^{-2} Hz^{-1}, is given by

$$N(f,T) = \frac{2\pi}{c^2} \frac{f^2}{e^{hf/kT} - 1}. \tag{4.3}$$

Having more carriers makes recombination more likely, so the photon flux (photons per second) depends on the concentrations of electrons and holes. This gives an exponential dependence on operating voltage for the recombination flux

$$F_{recomb,i} = e^{qV_i/kT} F_{darkrecomb,i} = e^{qV_i/kT} 2A \int_{E_{g,i}/h}^{\infty} f(x) N(f,T)\,\mathrm{d}f. \tag{4.4}$$

Thus the recombination current is

$$I_{recomb,i} = q e^{qV_i/kT} 2A \int_{E_{g,i}/h}^{\infty} N(f,T)\,\mathrm{d}f. \tag{4.5}$$

The total photon current comes from both the sunlight and photons from radiative recombination in neighboring layers. The solar photon flux incident on the *i*th layer (counting from the top) is given by

$$F_{solar,i} = f_\Omega A \int_{hc/E_{g,i-1}}^{hc/E_{g,i}} \frac{S(\lambda)}{E_{photon}(\lambda)}\,\mathrm{d}\lambda, \tag{4.6}$$

where f_Ω is a geometrical factor accounting for the solid angle occupied by the sun, $S(\lambda)$ is the AM1.5G solar spectrum in W m^{-2} nm^{-1} and E_{photon} is the energy of a photon of a given wavelength ($= hc/\lambda$). Concentrating sunlight is equivalent to the sun occupying a greater solid angle as seen by the solar cell, so f_Ω is increased to reflect increased concentration. For normal sunlight $f_\Omega = 1$. Concentrating the sunlight increases f_Ω up to a maximum value of 45730, where the sun would fill the entire 2π solid angle of the sky. The limits of integration are such because photons with energy below the band gap $E_{g,i}$ for that layer will not be absorbed, while photons with energy above $E_{g,i-1}$ will have already been absorbed by the upper layers.

Next, the photons reaching the *i*th layer due to radiative recombination can be calculated in a way similar to Eq. 4.4. A surface area of A instead of $2A$ is used because only one side of the layer sees the radiation from a given neighbor. The limits of integration are adjusted to only include photons that the *i*th layer is able to absorb. This yields

$$F_{neighbors,i} = e^{qV_{i-1}/kT} A \int_{E_{g,i-1}/h}^{\infty} N(f,T))\,\mathrm{d}f + e^{qV_{i+1}/kT} A \int_{E_{g,i}/h}^{\infty} N(f,T))\,\mathrm{d}f, \tag{4.7}$$

where the first and second terms must be removed for the top and bottom layers respectively.

By joining the two photon sources and converting photon flux into a current, we arrive at the total photon-generated current

$$I_{photon,i} = qf_{\Omega}A\int_{hc/E_{g,i-1}}^{hc/E_{g,i}} \frac{S(\lambda)}{E_{photon}(\lambda)}\,\mathrm{d}\lambda + qe^{qV_{i-1}/kT}A\int_{E_{g,i-1}/h}^{\infty} N(f,T))\,\mathrm{d}f + qe^{qV_{i+1}/kT}A\int_{E_{g,i}/h}^{\infty} N(f,T))\,\mathrm{d}f. \quad (4.8)$$

To solve for the optimal operating voltages, the electrical power across all n layers

$$P = \sum_{i=1}^{n} \left(I_{photon,i} - I_{recomb,i}\right) V_i \quad (4.9)$$

must be optimized numerically with respect to the voltages V_i for each layer. This is then compared to the incident solar power, taken by integrating over the entire solar spectrum while accounting for the area of the cell and the concentration of the sunlight

$$P_s = f_{\Omega}A\int_0^{\infty} S(\lambda)\,\mathrm{d}\lambda. \quad (4.10)$$

The AM1.5G spectrum ranges from 280-4000 nm, so those values are used as practical limits of integration in these calculations. Atmospheric absorption leaves negligible sunlight at shorter wavelengths and the black body spectrum dies of at longer wavelengths.

4.1.1 Numerically Solving the System of Equations

Mutual irradiance between the layers depends on their voltages, introducing coupling between neighbors. Maximizing electrical power then requires numerically solving a coupled system of nonlinear equations. Doing so requires good initial guesses of the operating voltage for each layer. Fortunately, the effects of mutual irradiance are small compared to the sunlight induced current, so solving the uncoupled system by ignoring the effects of mutual irradiance gives a close starting point for numerical solving. A single variable equation can then be easily solved to find the optimal

uncoupled operating voltage for the ith cell by

$$\left(1+\frac{qV_i}{kT}\right)e^{qV_i/kT}=\frac{F_{solar,i}}{F_{darkrecomb,i}}. \tag{4.11}$$

4.1.2 Parallel and Current-Matched Architectures

Layers in a multi-junction solar cell can either be connected in parallel or series circuits, each having certain advantages and disadvantages. Parallel circuits allow for each cell to operate at its optimal voltage, but each individual voltage is relatively low. On the other hand, series or current-matched circuits add together to output a single voltage as the sum of the operating voltages of each of the layers. All layers, however, must share a current, so the currents of all layers are limited by the lowest producing cell. Given a limited available library of materials, this results in some layers operating below their optimum voltage, bringing decreases in efficiency.

Numerically solving for optimal current-matched voltages begins as previously described. The operating voltages of each of the layers are then adjusted to match the current of the lowest producing layer. Both the recombination current (Eq. 4.4) and the mutual irradiance (Eq. 4.7) depend on voltage, so these values must be updated from the adjusted operating voltages. The optimal operating voltage of the current limiting layer is again solved for while holding all other voltages constant. This process is then iterated until converging to a uniform current and to constant values for the operating voltages of all cells.

4.2 Efficiency Calculation Results

4.2.1 Parallel Circuit

Following the method outlined in Section 4.1, we calculated the maximum efficiency from using Ti(O)OH, Fe(O)OH, Co(O)OH and Mn(O)OH with indirect gaps of 2.29, 2.14, 1.93, and

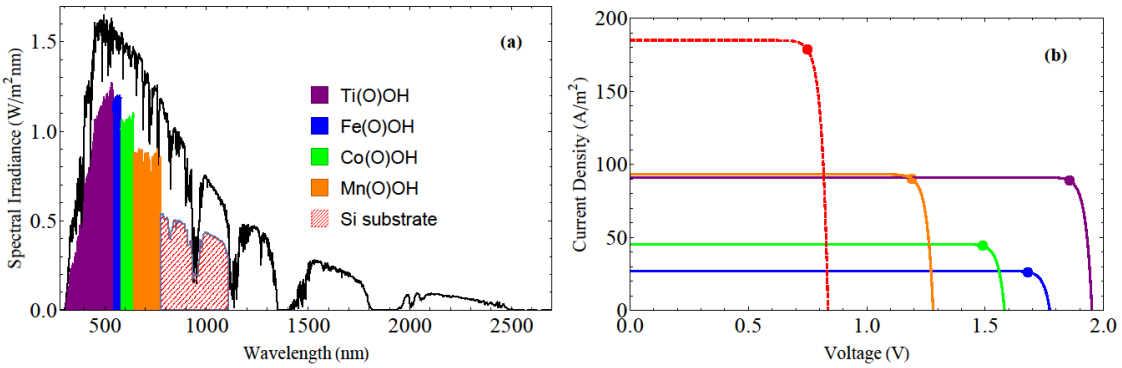

Figure 4.1 (a) Visual representation of maximum possible efficiency under normal sunlight for a ferritin-based multi-junction solar cell in a parallel configuration. The black envelope shows the AM1.5G solar spectrum and the heights of the color bands represent the efficiency at that wavelength. Thus the relative areas of the colored region versus the envelope represents the maximum total efficiency. If a low band gap material similar to silicon can be developed in ferritin, far greater efficiency can be realized. (b) I-V characteristic curves for each of the layers [colors correlate with part (a)] with points indicating where each layer must operate to obtain the maximum efficiency depicted in part (a). This figure is reproduced from [49].

1.60 eV respectively to be 38.0% for unconcentrated sunlight and 44.9% for maximally concentrated sunlight. These are obtained from operating voltages of 1.856, 1.680, 1.490, and 1.191 V for unconcentrated sunglight and 2.130, 1.954, 1.764 and 1.464 V for maximally concentrated sunlight. Fig. 4.1(a) graphically depicts the optimal efficiency for unconcentrated sunlight where the heights of the color bands correspond to the solar conversion efficiency at that wavelength. Fig. 4.1(b) shows the I-V characteristic curves for each layer and their appropriate maximum power points. Using only metal oxyhydroxides herein studied, the optimal efficiency of 38% already surpasses the Shockley-Queisser limit of 33.7% for a single junction solar cell, and is far greater than each type of nanocrystal could obtain individually from Ti(O)OH, Fe(O)OH, Co(O)OH, and Mn(O)OH (16.4%, 19.5%, 23.9%, and 29.9%, respectively).

While performing the calculations, we found the ferritin shell to have trivial impact on calculated efficiencies due to a lack of significant UV light past 4 eV in the AM1.5G solar spectrum.

Using the ferritin absorption as an upper energy bound, rather than simply the end of the spectrum, resulted in efficiency differences of less than one tenth of one percent. It is also possible that the electrons absorbed by the protein shell could themselves be harvested, though it is unclear if the absorption is taking place at the same location as conduction across the ferritin. Furthermore, we do not account for the possibility of multiple exciton generation, which has been shown more likely in quantum dots [40] and gives further increases in maximum possible efficiencies [41].

Having too high of a band gap for the bottom layer is the main factor limiting efficiencies in these calculations. The relatively high band gaps of all the metal oxyhydroxides studied leave too many photons unabsorbed for high efficiency. Having a final layer with a band gap similar to silicon's 1.12 eV would give large increases in efficiency, as can be seen by the size of the shaded region of Fig. 4.1(a). PbS nanocrystals are an excellent candidate for this, having already been synthesized within ferritin. Photoluminescence experiments showed a band gap around 1.1 eV for PbS in ferritin [13]. Using a final layer with such a band gap, efficiency limits rise to 51.3% for unconcentrated sunlight and 63.1% for maximally concentrated sunlight.

4.2.2 Current-Matched

The previous calculations assumed that each layer powers its own independent load, resulting in fairly low output voltages. Instead of each layer powering its own load, it is possible to connect the layers in electrical series, where the current in each cell must match all others. This results in much higher total output voltages, but introduces additional constraints on the system. Since each of the cells are connected in electrical series, the cell producing the lowest current will limit all others. Using the metal oxyhydroxides studied in this thesis, we calculate optimal efficiencies for a current matched solar cells derived from them. Due to the close band gaps of Ti(O)OH and Fe(O)OH, we eliminate Fe(O)OH from these calculations for a higher limiting current.

Using band gaps of 2.29, 193, 1.64, and 1.12 eV for Ti(O)OH, Co(O)OH, Mn(O)OH and

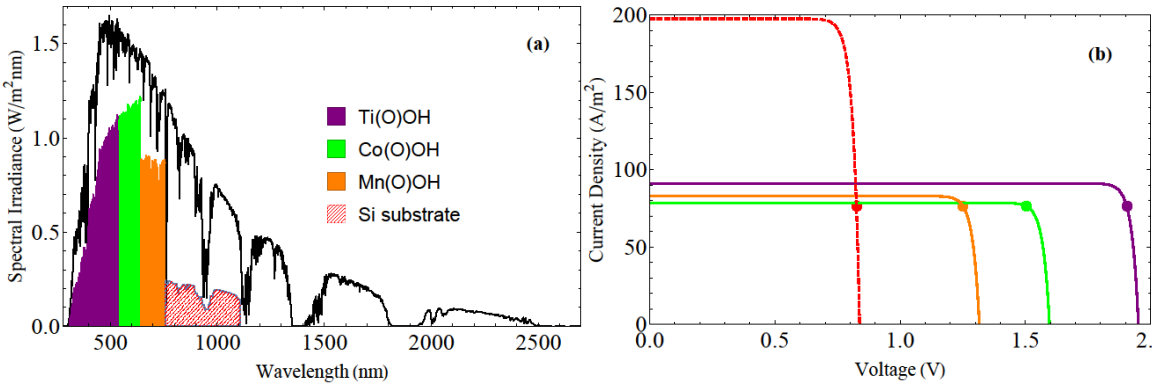

Figure 4.2 (a) Visual representation of maximum possible efficiency under normal sunlight for a ferritin-based multi-junction solar cell in a current matched configuration. The black envelope shows the AM1.5G solar spectrum and the heights of the color bands represent the efficiency at that wavelength. Thus the relative areas of the colored region versus the envelope represents the maximum total efficiency. If a low band gap material similar to silicon can be developed in ferritin, far greater efficiency can be realized. (b) I-V characteristic curves for each of the layers [colors correlate with part (a)] with points indicating where each layer must operate to obtain the maximum efficiency depicted in part (a). This figure is reproduced from [49].

silicon (or similar band gap material) we calculated a maximum current matched efficiency of 41.6% for unconcentrated sunlight and 50.0% for maximally concentrated sunlight, giving total operating voltages of 5.49 and 6.59 V. Again, Fig. 4.2(a) visually depicts the efficiency where the heights of the color bands represent the solar energy conversion efficiency of the solar cell at that wavelength. Fig. 4.2(b) shows the I-V characteristics for the different layers, with points marking where each layer must operate. Note that each layer is producing the same current. A summary of all calculated efficiencies is provided in Table 4.1.

Materials	f_Ω(# Suns)	Operating Voltages (V)	Theoretical Efficiency (%)
Ti,Fe,Co,Mn	1	1.856,1.680,1.490,1.181	38.0
	100	1.974,1.798,1.607,1.298	41.0
	Max	2.130,1.954,1.764,1.453	44.9
Ti,Fe,Co,Mn,Si	1	1.856,1.680,1.490,1.191,0.748	51.3
	100	1.974,1.798,1.608,1.308,0.846	56.4
	Max	2.130,1.954,1.764,1.464,1.012	63.1
Ti,Co,Mn,Si	1	1.905,1.505,1.251,0.825 (5.49 total)	41.6
(Current matched)	100	2.024,1.622,1.370,0.944 (5.96 total)	45.2
	Max	2.182,1.778,1.527,1.103 (6.59 total)	50.0

Table 4.1 Summary of efficiency calculation results. The first three rows only involve the ferritin-based metal oxyhydroxide nanocrystals whose band gaps we have measured. The next three rows incorporate a either silicon or a material with a similar band gap as the final layer. The final three rows use a silicon-like final layer, but in a current matched configuration where the total output voltage for the entire solar cell is also given. This table is reproduced from [49].

Chapter 5

Future Work and Conclusions

5.1 Future Work

Significant work must still be done to develop ferritin based nanocrystals for harvesting solar energy. As discussed in Section 4.2, a lack of low band gap materials is currently a main limiting factor. PbS is a strong candidate, though there are many other possibilities to explore. Many different types of II-VI semiconductors in ferritin remain to be explored. Preliminary work shows CdS to be a direct gap semiconductor with a band gap around 2.47 eV and FeS somewhere at or below 1.0 eV, making it another candidate for the final layer. Another advantage offered by II-VI materials is that they are primarily direct band gap semiconductors, absorbing light much more readily than the indirect materials studied in this thesis. Being direct gap semiconductors also makes characterization easier with photoluminescence.

In addition to having favorable band gaps, it must be possible to extract the excited electrons. Synthesizing gold nanoparticles on the outer surface has already shown this possible with native ferritin. Different materials likely will not differ in behavior. It also may be interesting to measure optical excitation lifetimes through either time correlated single photon counting or transient

absorption spectroscopy. In a solar cell, long excitation lifetimes would decrease radiative recombination from electrons relaxing before being carried away, even if there are barriers between the ferritin and electrode. Having an electrolyte that rapidly fills the holes could help extend these lifetimes.

Multiple exciton generation has been demonstrated in traditional colloidal quantum dots, but has yet to be proven specifically within ferritin. The protein shell may enhance or hinder this effect, so verification specific to ferritin should be investigated.

Comproportionation shows promise for synthesizing a new class of mixed metal oxides within ferritin. Preliminary results show that it can be used to make mixed metal oxide cores with iron, cobalt, and nickel. Perfecting this synthesis method could significantly expand our library of available materials, though it may not yield and band gaps significantly outside the range of the metal oxides already studied. Due to similar chemistry, it is likely that chromate can serve a similar purpose and lead to another class of mixed metal cores involving chromium.

5.2 Conclusions

Previous disagreements in the literature concerning the band gap of native ferritin have been reconciled. We found it to be an indirect gap semiconductor with a band gap of 2.14 eV, direct transitions beginning at 3.05 eV, and a 1.92 eV defect state. In studying reconstituted Fe(O)OH, we found that samples made with the TRIS pH buffer take up to two weeks to fully crystallize and reach a stable band gap. On the contrary, samples made with the imidazole buffer fully crystallized within a matter of hours.

By controlling the size and chemical composition of the nanocrystals, be it through different types of metal oxyhydroxides or co-depositing anions, we can tune the band gap of ferritin encapsulated nanocrystals over a range of 1.60-2.38 eV. These materials show great promise for solar

energy applications, and by themselves could reach solar energy conversion efficiencies as high as 38.0% under normal sunlight. Developing a low band gap final layer would give even greater increases in efficiency up to 51.3%.

Appendix A

Code for Efficiency Calculations

Here we include Mathematica code for calculating maximum efficiencies. The current matched code is a variation of the parallel circuit code, but iterated after adjusting to match the lowest current.

A.1 Parallel Circuit

```
SetDirectory[NotebookDirectory[]] ;
Clear["*"]
rawspectrum = Import["solar spectrum.csv"];
spectrum = Interpolation[rawspectrum];
```

Defining constants with high precision

```
prec = 20;
q = SetPrecision[1.6022*^-19, prec];
A = SetPrecision[1, prec]; (*surface area of cell*)
```

```
k = SetPrecision[8.6173*^-5, prec]; (* eV/K *)
Ts = SetPrecision[6000, prec];
Tc = SetPrecision[300, prec];
c = SetPrecision[2.998*^8, prec];
h = SetPrecision[4.1357*^-15, prec]; (* eV s *)
Eg = {SetPrecision[2.29, prec], SetPrecision[2.14, prec], SetPrecision[1.93, prec],
SetPrecision[1.6, prec], SetPrecision[1.12, prec]};
(*enter the band gaps for the different layers*)
fω = SetPrecision[1, prec]; (*45730formaximallyconcentratedsunlight,
1forunconcentrated.TakenfromtheDeVospaper*)
```

Solving initial guesses for coupled system of equations before redifining all of the fluxes to include coupling

```
n[f_, T_] = 2π/c^2 f^2/(Exp[hf/kT] - 1);
F01 = 2ANIntegrate[n[f, Tc], {f, Eg[[1]]/h, 100/h}];
Fs1 = fωANIntegrate[spectrum[λ] λ/(hcq) * 10^ - 9, {λ, 280, 1240/Eg[[1]]}] //Quiet;

F02 = 2ANIntegrate[n[f, Tc], {f, Eg[[2]]/h, 100/h}];
Fs2 = fωANIntegrate[spectrum[λ] λ/(hcq) * 10^ - 9, {λ, 1240/Eg[[1]], 1240/Eg[[2]]}] //Quiet;

F03 = 2ANIntegrate[n[f, Tc], {f, Eg[[3]]/h, 100/h}];
Fs3 = fωANIntegrate[spectrum[λ] λ/(hcq) * 10^ - 9, {λ, 1240/Eg[[2]], 1240/Eg[[3]]}] //Quiet;

F04 = 2ANIntegrate[n[f, Tc], {f, Eg[[4]]/h, 100/h}];
Fs4 = fωANIntegrate[spectrum[λ] λ/(hcq) * 10^ - 9, {λ, 1240/Eg[[3]], 1240/Eg[[4]]}] //Quiet;
```

```
F05 = 2ANIntegrate[n[f, Tc], {f, Eg[[5]]/h, 100/h}];
Fs5 = fωANIntegrate [spectrum[λ] λ/(hcq) * 10^ - 9, {λ, 1240/Eg[[4]], 1240/Eg[[5]]}] //Quiet;
NSolve [Reduce [(1 + x)Exp[x] == Fs1/F01, x, Reals], x] //Quiet;
x1init = x/.%[[1]];
NSolve [Reduce [(1 + x)Exp[x] == Fs2/F02, x, Reals], x] //Quiet;
x2init = x/.%[[1]];
NSolve [Reduce [(1 + x)Exp[x] == Fs3/F03, x, Reals], x] //Quiet;
x3init = x/.%[[1]];
NSolve [Reduce [(1 + x)Exp[x] == Fs4/F04, x, Reals], x] //Quiet;
x4init = x/.%[[1]];
NSolve [Reduce [(1 + x)Exp[x] == Fs5/F05, x, Reals], x] //Quiet;
x5init = x/.%[[1]];
```

Calculating photon fluxes

```
b1 = NIntegrate[n[f, Tc], {f, Eg[[1]]/h, 100/h}];
b2 = NIntegrate[n[f, Tc], {f, Eg[[2]]/h, 100/h}];
b3 = NIntegrate[n[f, Tc], {f, Eg[[3]]/h, 100/h}];
b4 = NIntegrate[n[f, Tc], {f, Eg[[4]]/h, 100/h}];
b5 = NIntegrate[n[f, Tc], {f, Eg[[5]]/h, 100/h}];
F01 = 2ANIntegrate[n[f, Tc], {f, Eg[[1]]/h, 100/h}];
Fs1 = fωANIntegrate [spectrum[λ] λ/(hcq) * 10^ - 9, {λ, 1240/4, 1240/Eg[[1]]}] + AExp[x2]b1//Quiet;

F02 = 2ANIntegrate[n[f, Tc], {f, Eg[[2]]/h, 100/h}];
Fs2 = fωANIntegrate [spectrum[λ] λ/(hcq) * 10^ - 9, {λ, 1240/Eg[[1]], 1240/Eg[[2]]}] + AExp[x1]b1+
```

$$A\text{Exp[x3]b2//Quiet;}$$

$$\text{F03} = 2A\text{NIntegrate}[n[f,\text{Tc}],\{f,\text{Eg[[3]]}/h,100/h\}];$$
$$\text{Fs3} = f\omega A\text{NIntegrate}\left[\text{spectrum}[\lambda]\frac{\lambda}{hcq} * 10\text{\^{}} - 9,\{\lambda,1240/\text{Eg[[2]]},1240/\text{Eg[[3]]}\}\right] + A\text{Exp[x2]b2+}$$

$$A\text{Exp[x4]b3//Quiet;}$$

$$\text{F04} = 2A\text{NIntegrate}[n[f,\text{Tc}],\{f,\text{Eg[[4]]}/h,100/h\}];$$
$$\text{Fs4} = f\omega A\text{NIntegrate}\left[\text{spectrum}[\lambda]\frac{\lambda}{hcq} * 10\text{\^{}} - 9,\{\lambda,1240/\text{Eg[[3]]},1240/\text{Eg[[4]]}\}\right] + A\text{Exp[x3]b3+}$$

$$A\text{Exp[x5]b4//Quiet;}$$

$$\text{F05} = 2A\text{NIntegrate}[n[f,\text{Tc}],\{f,\text{Eg[[5]]}/h,100/h\}];$$
$$\text{Fs5} = f\omega A\text{NIntegrate}\left[\text{spectrum}[\lambda]\frac{\lambda}{hcq} * 10\text{\^{}} - 9,\{\lambda,1240/\text{Eg[[4]]},1240/\text{Eg[[5]]}\}\right] + A\text{Exp[x4]b4//Quiet;}$$

Setting up the system of equations to find optimal operating voltages

$$\text{k2} = \frac{\text{NIntegrate}[n[f,\text{Tc}],\{f,\text{Eg[[1]]}/h,100/h\}]}{\text{NIntegrate}[n[f,\text{Tc}],\{f,\text{Eg[[2]]}/h,100/h\}]};$$
$$\text{k3} = \frac{\text{NIntegrate}[n[f,\text{Tc}],\{f,\text{Eg[[2]]}/h,100/h\}]}{\text{NIntegrate}[n[f,\text{Tc}],\{f,\text{Eg[[3]]}/h,100/h\}]};$$
$$\text{k4} = \frac{\text{NIntegrate}[n[f,\text{Tc}],\{f,\text{Eg[[3]]}/h,100/h\}]}{\text{NIntegrate}[n[f,\text{Tc}],\{f,\text{Eg[[4]]}/h,100/h\}]};$$
$$\text{k5} = \frac{\text{NIntegrate}[n[f,\text{Tc}],\{f,\text{Eg[[4]]}/h,100/h\}]}{\text{NIntegrate}[n[f,\text{Tc}],\{f,\text{Eg[[5]]}/h,100/h\}]};$$

$$\text{eqn1} = (1+\text{x1})\text{Exp[x1]} == \frac{\text{Fs1}}{\text{F01}} + \frac{1}{2}\text{x2Exp[x1]};$$
$$\text{eqn2} = (1+\text{x2})\text{Exp[x2]} == \frac{\text{Fs2}}{\text{F02}} + \frac{1}{2}\text{x1Exp[x2]k2} + \frac{1}{2}\text{x3Exp[x2]};$$

$$\text{eqn3} = (1+\text{x3})\text{Exp}[\text{x3}] == \frac{\text{Fs3}}{\text{F03}} + \frac{1}{2}\text{x2Exp}[\text{x3}]\text{k3} + \frac{1}{2}\text{x4Exp}[\text{x3}];$$

$$\text{eqn4} = (1+\text{x4})\text{Exp}[\text{x4}] == \frac{\text{Fs4}}{\text{F04}} + \frac{1}{2}\text{x3Exp}[\text{x4}]\text{k4} + \frac{1}{2}\text{x5Exp}[\text{x4}];$$

$$\text{eqn5} = (1+\text{x5})\text{Exp}[\text{x5}] == \frac{\text{Fs5}}{\text{F05}} + \frac{1}{2}\text{x4Exp}[\text{x5}]\text{k5};$$

Solving the system

$$\text{voltages} =$$

$$\text{FindRoot}[\{\text{eqn1}, \text{eqn2}, \text{eqn3}, \text{eqn4}, \text{eqn5}\},$$

$$\{\{\text{x1}, \text{x1init}\}, \{\text{x2}, \text{x2init}\}, \{\text{x3}, \text{x3init}\}, \{\text{x4}, \text{x4init}\}, \{\text{x5}, \text{x5init}\}\}, \text{WorkingPrecision} \to \text{prec},$$

$$\text{AccuracyGoal} \to 8, \text{PrecisionGoal} \to 8, \text{MaxIterations} \to 1000]//\text{Quiet};$$

$$\text{x1} = \text{x1}/.\text{voltages};$$

$$\text{x2} = \text{x2}/.\text{voltages};$$

$$\text{x3} = \text{x3}/.\text{voltages};$$

$$\text{x4} = \text{x4}/.\text{voltages};$$

$$\text{x5} = \text{x5}/.\text{voltages};$$

$$\text{V1} = k\text{Tcx1}$$

$$\text{V2} = k\text{Tcx2}$$

$$\text{V3} = k\text{Tcx3}$$

$$\text{V4} = k\text{Tcx4}$$

$$\text{V5} = k\text{Tcx5}$$

Calculating incident solar power and efficiency of the multi-junction cell

$$\text{sunpower} = \text{f}\omega A\text{NIntegrate}[\text{spectrum}[\lambda], \{\lambda, 280, 4000\}]//\text{Quiet}$$

$$\text{cell1} = (-\text{x1} * k * \text{Tc} * (q\text{F01}(\text{Exp}[\text{x1}] - 1) - q(\text{Fs1} - \text{F01})))$$

$$\text{cell2} = (-\text{x2} * k * \text{Tc} * (q\text{F02}(\text{Exp}[\text{x2}] - 1) - q(\text{Fs2} - \text{F02})))$$

$$\text{cell3} = (-\text{x3} * k * \text{Tc} * (q\text{F03}(\text{Exp}[\text{x3}] - 1) - q(\text{Fs3} - \text{F03})))$$

```
cell4 = (-x4 * k * Tc * (qF04(Exp[x4] - 1) - q(Fs4 - F04)))
cell5 = (-x5 * k * Tc * (qF05(Exp[x5] - 1) - q(Fs5 - F05)))
(cell1+cell2+cell3+cell4+cell5)/sunpower
```

Plots

Calculating weighting factors to make figure (a) a better approximation

```
w1 = cell1 / (fωANIntegrate[(spectrum[λ]/hc) λ * 10^ - 9 * kTcx1, {λ, 1240/4, 1240/Eg[[1]]}]) ;
w2 = cell2 / (fωANIntegrate[(spectrum[λ]/hc) λ * 10^ - 9 * kTcx2, {λ, 1240/Eg[[1]], 1240/Eg[[2]]}]) ;
w3 = cell3 / (fωANIntegrate[(spectrum[λ]/hc) λ * 10^ - 9 * kTcx3, {λ, 1240/Eg[[2]], 1240/Eg[[3]]}]) ;
w4 = cell4 / (fωANIntegrate[(spectrum[λ]/hc) λ * 10^ - 9 * kTcx4, {λ, 1240/Eg[[3]], 1240/Eg[[4]]}]) ;
w5 = cell5 / (fωANIntegrate[(spectrum[λ]/hc) λ * 10^ - 9 * kTcx5, {λ, 1240/Eg[[4]], 1240/Eg[[5]]}]) ;
```

Spectrum

```
figa = Graphics[Text[Style["(a)", FontSize → 20, FontWeight → Bold], {2500, 1.5}]];
figb = Graphics[Text[Style["(b)", FontSize → 20, FontWeight → Bold], {1.8, 175}]];
labels = {Graphics[{Purple, Rectangle[{0,0}, {1,1}]}], Graphics[{Blue, Rectangle[{0,0}, {1,1}]}],
Graphics[{Green, Rectangle[{0,0}, {1,1}]}], Graphics[{Orange, Rectangle[{0,0}, {1,1}]}],
Graphics[{EdgeForm[{Thickness[.05], Red}], White, Rectangle[{0,0}, {1,1}], Red,
Thickness[.02], Line[{{0,0}, {1,1}}], Line[{{0, .2}, {.8,1}}], Line[{{0, .4}, {.6,1}}],
Line[{{0, .6}, {.4,1}}], Line[{{0, .8}, {.2,1}}], Line[{{.2,0}, {1, .8}}],
Line[{{.4,0}, {1, .6}}], Line[{{.6,0}, {1, .4}}], Line[{{.8,0}, {1, .2}}]}];
Specplot = Plot[spectrum[λ], {λ, 280, 2700}, PlotStyle → Black, Frame → True,
PlotRange → {{280, 2700}, {0, 1.7}}, ImageSize → 600,
FrameLabel → {Style["Wavelength (nm)", FontSize → 20],
Style ["Spectral Irradiance (W/m^2nm)", FontSize → 20, SingleLetterItalics → False]},
```

```
LabelStyle → Large,
(*PlotLabel → Style["Solar Energy Conversion from a Ferritin-based PV Cell", FontSize → 20, Bold], *)
PlotLegends → Placed[SwatchLegend[{Purple, Blue, Green, Orange, Red},
{Style["Ti(O)OH", FontSize → 20], Style["Fe(O)OH", FontSize → 20], Style["Co(O)OH", FontSize → 20],
Style["Mn(O)OH", FontSize → 20], Style["Si substrate", FontSize → 20]}, LegendMarkerSize → 20,
LegendMarkers → labels], {Center, Right}]];
plot1 = Plot [w1 spectrum[λ]/hc λ * 10^ - 9 * kTcx1, {λ, 1240/4, 1240/Eg[[1]]}, PlotRange → {0, 1.5},
PlotStyle → Purple, Filling → Axis, FillingStyle → Purple];
plot2 = Plot [w2 spectrum[λ]/hc λ * 10^ - 9 * kTcx2, {λ, 1240/Eg[[1]], 1240/Eg[[2]]}, PlotRange → {0, 1.5},
Filling → Axis, PlotStyle → Blue, FillingStyle → Blue];
plot3 = Plot [w3 spectrum[λ]/hc λ * 10^ - 9 * kTcx3, {λ, 1240/Eg[[2]], 1240/Eg[[3]]}, PlotRange → {0, 1.5},
PlotStyle → Green, Filling → Axis, FillingStyle → Green];
plot4 = Plot [w4 spectrum[λ]/hc λ * 10^ - 9 * kTcx4, {λ, 1240/Eg[[3]], 1240/Eg[[4]]}, PlotRange → {0, 1.5},
PlotStyle → Orange, Filling → Axis, FillingStyle → Orange];
plot5 = Plot [w5 spectrum[λ]/hc λ * 10^ - 9 * kTcx5, {λ, 1240/Eg[[4]], 1240/Eg[[5]]}, PlotRange → {0, 1.5},
PlotStyle → Red, Filling → Axis, FillingStyle → Red];
plot5 = RegionPlot [((λ < 1240/Eg[[5]]) && (λ > 1240/Eg[[4]]) && (y < w5 spectrum[λ]/hc λ * 10^ - 9 * kTcx5)),
{λ, 280, 2700/Eg[[5]]}, {y, 0, 1.7}, PlotStyle → Red, PlotPoints → 100, Mesh → 30,
MeshFunctions → {#1 - 800#2 &}, MeshShading → {None}, MeshStyle → Red];
Show[Specplot, plot1, plot2, plot3, plot4, plot5, figa]
```

I-V characteristics

Note that axes are set for unconcentrated sunlight. Concentrated sunlight will need different scales.

```
characteristics =
Plot[{-(qF01 (Exp[V/kTc] - 1) - q(Fs1 - F01)), -(qF02 (Exp[V/kTc] - 1) - q(Fs2 - F02)),
-(qF03 (Exp[V/kTc] - 1) - q(Fs3 - F03)), -(qF04 (Exp[V/kTc] - 1) - q(Fs4 - F04)),
-(qF05 (Exp[V/kTc] - 1) - q(Fs5 - F05))}, {V, 0, 2}, PlotRange → {0, 200},
PlotStyle → {{Purple, Thick}, {Blue, Thick}, {Green, Thick}, {Orange, Thick}, {Red, Thick, Dashed}}];
points1 = {{kTcx1, -(qF01 (Exp[kTcx1/kTc] - 1) - q(Fs1 - F01))}};
points2 = {{kTcx2, -(qF02 (Exp[kTcx2/kTc] - 1) - q(Fs2 - F02))}};
points3 = {{kTcx3, -(qF03 (Exp[kTcx3/kTc] - 1) - q(Fs3 - F03))}};
points4 = {{kTcx4, -(qF04 (Exp[kTcx4/kTc] - 1) - q(Fs4 - F04))}};
points5 = {{kTcx5, -(qF05 (Exp[kTcx5/kTc] - 1) - q(Fs5 - F05))}};
pointsplot = ListPlot[{points1, points2, points3, points4, points5}, PlotRange → {{0, 2}, {0, 200}},
PlotStyle → {{Purple, PointSize[.02]}, {Blue, PointSize[.02]}, {Green, PointSize[.02]},
{Orange, PointSize[.02]}, {Red, PointSize[.02]}}, Frame → True, ImageSize → 600,
FrameLabel → {Style["Voltage (V)", FontSize → 20],
 Style["Current Density (A/m^2)", FontSize → 20, SingleLetterItalics → False]}, LabelStyle → Large];
figb = Graphics[Text[Style["(b)", FontSize → 20, FontWeight → Bold], {1.8, 175}]];
Show[pointsplot, characteristics, figb]
```

A.2 Current-Matched

```
SetDirectory[NotebookDirectory[]] ;
Clear["*"]
rawspectrum = Import["solar spectrum.csv"];
spectrum = Interpolation[rawspectrum];
```

Defining constants with high precision

```
prec = 20;
q = SetPrecision[1.6022*^-19, prec];
A = SetPrecision[1, prec]; (*surface area of cell*)
k = SetPrecision[8.6173*^-5, prec]; (* eV/K *)
Ts = SetPrecision[6000, prec];
Tc = SetPrecision[300, prec];
c = SetPrecision[2.998*^8, prec];
h = SetPrecision[4.1357*^-15, prec]; (* eV s *)
Eg = {SetPrecision[2.29, prec], SetPrecision[1.93, prec], SetPrecision[1.64, prec],
SetPrecision[1.12, prec]}; (*enter the band gaps for the different layers*)
fω = SetPrecision[1, prec]; (*45730formaximallyconcentratedsunlightand1for
unconcentratedsunlight.TakenfromtheDeVospaper*)
```

Solving initial guesses for coupled system of equations before redifining all of the fluxes to include coupling

```
n[f_, T_] = 2π/c^2 f^2/(Exp[hf/kT] - 1);
F01 = 2ANIntegrate[n[f, Tc], {f, Eg[[1]]/h, 100/h}];
Fs1 = fωANIntegrate [spectrum[λ] λ/(hcq) * 10^ - 9, {λ, 280, 1240/Eg[[1]]}] //Quiet;

F02 = 2ANIntegrate[n[f, Tc], {f, Eg[[2]]/h, 100/h}];
Fs2 = fωANIntegrate [spectrum[λ] λ/(hcq) * 10^ - 9, {λ, 1240/Eg[[1]], 1240/Eg[[2]]}] //Quiet;

F03 = 2ANIntegrate[n[f, Tc], {f, Eg[[3]]/h, 100/h}];
```

```
Fs3 = fωANIntegrate[spectrum[λ] λ/(hcq) * 10^ - 9, {λ, 1240/Eg[[2]], 1240/Eg[[3]]}] //Quiet;

F04 = 2ANIntegrate[n[f, Tc], {f, Eg[[4]]/h, 100/h}];
Fs4 = fωANIntegrate[spectrum[λ] λ/(hcq) * 10^ - 9, {λ, 1240/Eg[[3]], 1240/Eg[[4]]}] //Quiet;

NSolve[Reduce[(1 + x)Exp[x] == Fs1/F01, x, Reals], x] //Quiet;
x1init = x/.%[[1]];
NSolve[Reduce[(1 + x)Exp[x] == Fs2/F02, x, Reals], x] //Quiet;
x2init = x/.%[[1]];
NSolve[Reduce[(1 + x)Exp[x] == Fs3/F03, x, Reals], x] //Quiet;
x3init = x/.%[[1]];
NSolve[Reduce[(1 + x)Exp[x] == Fs4/F04, x, Reals], x] //Quiet;
x4init = x/.%[[1]];
```

Calculating photon fluxes

```
b1 = NIntegrate[n[f, Tc], {f, Eg[[1]]/h, 100/h}];
b2 = NIntegrate[n[f, Tc], {f, Eg[[2]]/h, 100/h}];
b3 = NIntegrate[n[f, Tc], {f, Eg[[3]]/h, 100/h}];
b4 = NIntegrate[n[f, Tc], {f, Eg[[4]]/h, 100/h}];
F01 = 2ANIntegrate[n[f, Tc], {f, Eg[[1]]/h, 100/h}];
Fs1 = fωANIntegrate[spectrum[λ] λ/(hcq) * 10^ - 9, {λ, 1240/4, 1240/Eg[[1]]}] + AExp[x2]b1//Quiet;

F02 = 2ANIntegrate[n[f, Tc], {f, Eg[[2]]/h, 100/h}];
Fs2 = fωANIntegrate[spectrum[λ] λ/(hcq) * 10^ - 9, {λ, 1240/Eg[[1]], 1240/Eg[[2]]}] + AExp[x1]b1+
```

$$A\text{Exp[x3]b2//Quiet;}$$

$$\text{F03} = 2A\text{NIntegrate}[n[f,\text{Tc}],\{f,\text{Eg[[3]]}/h,100/h\}];$$

$$\text{Fs3} = f\omega A\text{NIntegrate}\left[\text{spectrum}[\lambda]\frac{\lambda}{hcq} * 10\text{\^{}} - 9,\{\lambda,1240/\text{Eg[[2]]},1240/\text{Eg[[3]]}\}\right] + A\text{Exp[x2]b2+}$$

$$A\text{Exp[x4]b3//Quiet;}$$

$$\text{F04} = 2A\text{NIntegrate}[n[f,\text{Tc}],\{f,\text{Eg[[4]]}/h,100/h\}];$$

$$\text{Fs4} = f\omega A\text{NIntegrate}\left[\text{spectrum}[\lambda]\frac{\lambda}{hcq} * 10\text{\^{}} - 9,\{\lambda,1240/\text{Eg[[3]]},1240/\text{Eg[[4]]}\}\right] + A\text{Exp[x3]b3//Quiet;}$$

Setting up the system of equations to find optimal operating voltages

$$\text{k2} = \frac{\text{NIntegrate}[n[f,\text{Tc}],\{f,\text{Eg[[1]]}/h,100/h\}]}{\text{NIntegrate}[n[f,\text{Tc}],\{f,\text{Eg[[2]]}/h,100/h\}]};$$

$$\text{k3} = \frac{\text{NIntegrate}[n[f,\text{Tc}],\{f,\text{Eg[[2]]}/h,100/h\}]}{\text{NIntegrate}[n[f,\text{Tc}],\{f,\text{Eg[[3]]}/h,100/h\}]};$$

$$\text{k4} = \frac{\text{NIntegrate}[n[f,\text{Tc}],\{f,\text{Eg[[3]]}/h,100/h\}]}{\text{NIntegrate}[n[f,\text{Tc}],\{f,\text{Eg[[4]]}/h,100/h\}]};$$

$$\text{eqn1} = (1+\text{x1})\text{Exp[x1]} == \frac{\text{Fs1}}{\text{F01}} + \frac{1}{2}\text{x2Exp[x1]};$$

$$\text{eqn2} = (1+\text{x2})\text{Exp[x2]} == \frac{\text{Fs2}}{\text{F02}} + \frac{1}{2}\text{x1Exp[x2]k2} + \frac{1}{2}\text{x3Exp[x2]};$$

$$\text{eqn3} = (1+\text{x3})\text{Exp[x3]} == \frac{\text{Fs3}}{\text{F03}} + \frac{1}{2}\text{x2Exp[x3]k3} + \frac{1}{2}\text{x4Exp[x3]};$$

$$\text{eqn4} = (1+\text{x4})\text{Exp[x4]} == \frac{\text{Fs4}}{\text{F04}} + \frac{1}{2}\text{x3Exp[x4]k4;}$$

Solving the system

$$\text{voltages} = \text{FindRoot}[\{\text{eqn1},\text{eqn2},\text{eqn3},\text{eqn4}\},\{\{\text{x1},\text{x1init}\},\{\text{x2},\text{x2init}\},\{\text{x3},\text{x3init}\},\{\text{x4},\text{x4init}\}\},$$

$$\text{WorkingPrecision} \to \text{prec},\text{AccuracyGoal} \to 8,\text{PrecisionGoal} \to 8,\text{MaxIterations} \to 1000]\text{//Quiet;}$$

$$\text{x1} = \text{x1/.voltages}$$

```
x2 = x2/.voltages
x3 = x3/.voltages
x4 = x4/.voltages
V1 = kTcx1
V2 = kTcx2
V3 = kTcx3
V4 = kTcx4
I1 = q(Fs1 - F01Exp[x1])
I2 = q(Fs2 - F02Exp[x2])
I3 = q(Fs3 - F03Exp[x3])
I4 = q(Fs4 - F04Exp[x4])
```

Efficiency of a 4 layer non current matched cell

```
sunpower = fωANIntegrate[spectrum[λ], {λ, 280, 4000}]//Quiet;
cell1 = (-x1 * k * Tc * (qF01(Exp[x1] - 1) - q(Fs1 - F01)));
cell2 = (-x2 * k * Tc * (qF02(Exp[x2] - 1) - q(Fs2 - F02)));
cell3 = (-x3 * k * Tc * (qF03(Exp[x3] - 1) - q(Fs3 - F03)));
cell4 = (-x4 * k * Tc * (qF04(Exp[x4] - 1) - q(Fs4 - F04)));
(cell1+cell2+cell3+cell4)/sunpower
```

0.506954

Note that these only serve as starting points. The cell will be limited by the lowest current, which with our given materials looks to be the second layer. Since the voltage of the surround cells must change to obtain that current, that will slightly influence the optimal voltage for the limiting cell, so we take an iterative approach. For some reason, a for loop (Do function) wasn't working, but copying and pasting the code a bunch of time was, so here is my sloppy version.

Iterative "for" loop

When writing this code, I had all kinds of trouble getting *Mathematica* to cooperate with a Do loop, so eventually I just settled on copying and pasting the code below twenty times. I only include one instance, so add as many copies as you deem necessary.

```
current = q(Fs2 - F02Exp[x2]);
lh1 = q(Fs1 - F01Exp[x1p]);
lh3 = q(Fs3 - F03Exp[x3p]);
lh4 = q(Fs4 - F04Exp[x4p]);
x1init = x1;
x3init = x3;
x4init = x4;
(*Setvoltagesofothercellsbasedontheir I - V characteristics*)
FindRoot[lh1 == current, {x1p, x1init}];
x1 = x1p/.%;
FindRoot[lh3 == current, {x3p, x3init}];
x3 = x3p/.%;
FindRoot[lh4 == current, {x4p, x4init}];
x4 = x4p/.%;
(*Redefine the photon fluxes based on the new operating voltages*)
Fs1 = fωANIntegrate [spectrum[λ] λ/(hcq) * 10^ - 9, {λ, 1240/4, 1240/Eg[[1]]}] + AExp[x2]b1//Quiet;

Fs2 = fωANIntegrate [spectrum[λ] λ/(hcq) * 10^ - 9, {λ, 1240/Eg[[1]], 1240/Eg[[2]]}] + AExp[x1]b1+

AExp[x3]b2//Quiet;
```

$$\text{Fs3} = \text{f}\omega A\text{NIntegrate}\left[\text{spectrum}[\lambda]\frac{\lambda}{hcq} * 10\text{\^{}} - 9, \{\lambda, 1240/\text{Eg}[[2]], 1240/\text{Eg}[[3]]\}\right] + A\text{Exp}[\text{x2}]\text{b2} +$$

$$A\text{Exp}[\text{x4}]\text{b3//Quiet};$$

$$\text{Fs4} = \text{f}\omega A\text{NIntegrate}\left[\text{spectrum}[\lambda]\frac{\lambda}{hcq} * 10\text{\^{}} - 9, \{\lambda, 1240/\text{Eg}[[3]], 1240/\text{Eg}[[4]]\}\right] + A\text{Exp}[\text{x3}]\text{b3//Quiet};$$

(*Find the new optimal voltage for the limiting cell based on the updated neighboring voltages*)

$$\text{FindRoot}\left[(1 + \text{x2p})\text{Exp}[\text{x2p}] == \frac{\text{Fs2}}{\text{F02}} + \frac{1}{2}\text{x1Exp}[\text{x2p}]\text{k2} + \frac{1}{2}\text{x3Exp}[\text{x2p}], \{\text{x2p}, \text{x2}\}\right]\text{//Quiet};$$

$$\text{x2} = \text{x2p}/.\%;$$

x1

x2

x3

x4

Check that currents match

$$q(\text{Fs1} - \text{F01Exp}[\text{x1}])$$

$$q(\text{Fs2} - \text{F02Exp}[\text{x2}])$$

$$q(\text{Fs3} - \text{F03Exp}[\text{x3}])$$

$$q(\text{Fs4} - \text{F04Exp}[\text{x4}])$$

Calculating incident solar power and efficiency of the multi-junction cell

$$\text{sunpower} = \text{f}\omega A\text{NIntegrate}[\text{spectrum}[\lambda], \{\lambda, 280, 4000\}]\text{//Quiet}$$

$$\text{cell1} = (-\text{x1} * k * \text{Tc} * (q\text{F01}(\text{Exp}[\text{x1}] - 1) - q(\text{Fs1} - \text{F01})))$$

$$\text{cell2} = (-\text{x2} * k * \text{Tc} * (q\text{F02}(\text{Exp}[\text{x2}] - 1) - q(\text{Fs2} - \text{F02})))$$

$$\text{cell3} = (-\text{x3} * k * \text{Tc} * (q\text{F03}(\text{Exp}[\text{x3}] - 1) - q(\text{Fs3} - \text{F03})))$$

$$\text{cell4} = (-\text{x4} * k * \text{Tc} * (q\text{F04}(\text{Exp}[\text{x4}] - 1) - q(\text{Fs4} - \text{F04})))$$

$$\frac{\text{cell1}+\text{cell2}+\text{cell3}+\text{cell4}}{\text{sunpower}}$$

$k\text{Tcx1}$

$k\text{Tcx2}$

$k\text{Tcx3}$

$k\text{Tcx4}$

$k\text{Tc}(\text{x1}+\text{x2}+\text{x3}+\text{x4})$

Plots

Calculating weighting factors to make figure (a) a better approximation

$$\text{w1} = \text{cell1} \Big/ \left(\text{f}\omega A\text{NIntegrate}\left[\frac{\text{spectrum}[\lambda]}{hc}\lambda * 10\text{^} - 9 * k\text{Tcx1}, \{\lambda, 1240/4, 1240/\text{Eg}[[1]]\}\right]\right);$$
$$\text{w2} = \text{cell2} \Big/ \left(\text{f}\omega A\text{NIntegrate}\left[\frac{\text{spectrum}[\lambda]}{hc}\lambda * 10\text{^} - 9 * k\text{Tcx2}, \{\lambda, 1240/\text{Eg}[[1]], 1240/\text{Eg}[[2]]\}\right]\right);$$
$$\text{w3} = \text{cell3} \Big/ \left(\text{f}\omega A\text{NIntegrate}\left[\frac{\text{spectrum}[\lambda]}{hc}\lambda * 10\text{^} - 9 * k\text{Tcx3}, \{\lambda, 1240/\text{Eg}[[2]], 1240/\text{Eg}[[3]]\}\right]\right);$$
$$\text{w4} = \text{cell4} \Big/ \left(\text{f}\omega A\text{NIntegrate}\left[\frac{\text{spectrum}[\lambda]}{hc}\lambda * 10\text{^} - 9 * k\text{Tcx4}, \{\lambda, 1240/\text{Eg}[[3]], 1240/\text{Eg}[[4]]\}\right]\right);$$

Spectrum

```
figa = Graphics[Text[Style["(a)", FontSize → 20, FontWeight → Bold], {2500, 1.5}]];
figb = Graphics[Text[Style["(b)", FontSize → 20, FontWeight → Bold], {1.8, 175}]];
labels = {Graphics[{Purple, Rectangle[{0, 0}, {1, 1}]}], Graphics[{Green, Rectangle[{0, 0}, {1, 1}]}],
Graphics[{Orange, Rectangle[{0, 0}, {1, 1}]}],
Graphics[{EdgeForm[{Thickness[.05], Red}], White, Rectangle[{0, 0}, {1, 1}], Red,
Thickness[.02], Line[{{0, 0}, {1, 1}}], Line[{{0, .2}, {.8, 1}}], Line[{{0, .4}, {.6, 1}}],
Line[{{0, .6}, {.4, 1}}], Line[{{0, .8}, {.2, 1}}], Line[{{.2, 0}, {1, .8}}],
Line[{{.4, 0}, {1, .6}}], Line[{{.6, 0}, {1, .4}}], Line[{{.8, 0}, {1, .2}}]]};
Specplot = Plot[spectrum[λ], {λ, 280, 2700}, PlotStyle → Black, Frame → True,
PlotRange → {{280, 2700}, {0, 1.7}}, ImageSize → 600,
```

```
FrameLabel → {Style["Wavelength (nm)", FontSize → 20],
Style["Spectral Irradiance (W/m^2nm)", FontSize → 20, SingleLetterItalics → False]},
LabelStyle → Large,
PlotLegends → Placed[SwatchLegend[{Purple, Green, Orange, Red},
{Style["Ti(O)OH", FontSize → 20], Style["Co(O)OH", FontSize → 20], Style["Mn(O)OH", FontSize → 20],
Style["Si substrate", FontSize → 20]}, LegendMarkerSize → 20, LegendMarkers → labels],
{Center, Right}]];
plot1 = Plot[w1 spectrum[λ]/hc λ * 10^ - 9 * kTcx1, {λ, 1240/4, 1240/Eg[[1]]}, PlotRange → {0, 1.5},
PlotStyle → Purple, Filling → Axis, FillingStyle → Purple];
plot2 = Plot[w2 spectrum[λ]/hc λ * 10^ - 9 * kTcx2, {λ, 1240/Eg[[1]], 1240/Eg[[2]]}, PlotRange → {0, 1.5},
Filling → Axis, PlotStyle → Green, FillingStyle → Green];
plot3 = Plot[w3 spectrum[λ]/hc λ * 10^ - 9 * kTcx3, {λ, 1240/Eg[[2]], 1240/Eg[[3]]}, PlotRange → {0, 1.5},
PlotStyle → Orange, Filling → Axis, FillingStyle → Orange];
plot4 = Plot[w4 spectrum[λ]/hc λ * 10^ - 9 * kTcx4, {λ, 1240/Eg[[3]], 1240/Eg[[4]]}, PlotRange → {0, 1.5},
PlotStyle → Red, Filling → Axis, FillingStyle → Red];
plot4 = RegionPlot[((λ < 1240/Eg[[4]]) && (λ > 1240/Eg[[3]]) && (y < w4 spectrum[λ]/hc λ * 10^ - 9 * kTcx4)),
{λ, 280, 2700}, {y, 0, 1.7}, PlotStyle → Red, PlotPoints → 100, Mesh → 30, MeshFunctions → {#1 - 800#2 &},
MeshShading → {None}, MeshStyle → Red];
Show[Specplot, plot1, plot2, plot3, plot4, figa]
```

I-V characteristics

```
characteristics =
Plot[{-(qF01 (Exp[V/kTc] - 1) - q(Fs1 - F01)), -(qF02 (Exp[V/kTc] - 1) - q(Fs2 - F02)),
-(qF03 (Exp[V/kTc] - 1) - q(Fs3 - F03)), -(qF04 (Exp[V/kTc] - 1) - q(Fs4 - F04))}, {V, 0, 2},
PlotRange → {0, 200},
```

```
PlotStyle → {{Purple, Thick}, {Green, Thick}, {Orange, Thick}, {Red, Thick, Dashed}}];
points1 = {{kTcx1, -(qF01 (Exp[kTcx1/kTc] - 1) - q(Fs1 - F01))}};
points2 = {{kTcx2, -(qF02 (Exp[kTcx2/kTc] - 1) - q(Fs2 - F02))}};
points3 = {{kTcx3, -(qF03 (Exp[kTcx3/kTc] - 1) - q(Fs3 - F03))}};
points4 = {{kTcx4, -(qF04 (Exp[kTcx4/kTc] - 1) - q(Fs4 - F04))}};
pointsplot = ListPlot[{points1, points2, points3, points4}, PlotRange → {{0, 2}, {0, 200}},
PlotStyle → {{Purple, PointSize[.02]}, {Green, PointSize[.02]}, {Orange, PointSize[.02]},
{Red, PointSize[.02]}}, Frame → True, ImageSize → 600,
FrameLabel → {Style["Voltage (V)", FontSize → 20],
 Style["Current Density (A/m^2)", FontSize → 20, SingleLetterItalics → False]}, LabelStyle → Large];
figb = Graphics[Text[Style["(b)", FontSize → 20, FontWeight → Bold], {1.8, 175}]];
Show[pointsplot, characteristics, figb]
```

Bibliography

[1] As calculated by integrating the AM1.5G power spectrum over the visible region from 390-700 nm and dividing by the total incident power.

[2] C. Kittel, *Introduction to Solid State Physics*, 8th ed. (John Wiley and Sons, Hoboken NJ, 2005), pp. 188–189.

[3] P. Allen and M. Cardona, "Temperature dependence of the direct gap of Si and Ge," Phys. Rev. B. **27,** 4760–4769 (1983).

[4] S. Granick and L. Michaelis, "Ferritin and Apoferritin," Science **95,** 439–440 (1942).

[5] T. Douglas and V. Stark, "Nanophase Cobalt Oxyhydroxide Mineral Synthesized within the Protein Cage of Ferritin," Inorg. Chem. **39,** 1828–1830 (2000).

[6] M. Klem, J. Mosolf, M. Young, and T. Douglas, "Photochemical Mineralization of Europium, Titanium, and Iron Oxyhydroxide Nanoparticles in the Ferritin Protein Cage," Inorg. Chem. **47,** 2237–2239 (2008).

[7] P. Mackel, J. Charnock, C. Garner, F. Meldrum, and S. Mann, "Characterization of the Manganese Core of Reconstituted Ferritin by X-ray Absorption Spectroscopy," J. Am. Chem. Soc. **115,** 8471–8472 (1993).

[8] F. Meldrum, T. Douglas, S. Levi, P. Arosio, and S. Mann, "Reconstitution of manganese oxide cores in horse spleen and recombinant ferritins," J. Inorg. Biochem. **58,** 59–68 (1995).

[9] M. Okuda, K. Iwahori, I. Yamashita, and H. Yoshimura, "Fabrication of nickel and chromium nanoparticles using the protein cage of apoferritin," Biotechnol Bioeng. **84,** 187–194 (2003).

[10] J. Polanams, A. Ray, and R. Watt, "Nanophase iron phosphate, iron arsenate, iron vanadate, and iron molybdate minerals synthesized within the protein cage of ferritin," Inorg. Chem. **44,** 3203–3209 (2005).

[11] K. Wong and S. Mann, "Biomimetic synthesis of cadmium sulfide-ferritin nanoparticles," Adv. Mater. **8,** 928–932 (1996).

[12] T. Douglas, D. Dickson, S. Betteridge, J. Charnock, C. Garner, and S. Mann, "Synthesis and Structure of an Iron(III) Sulfide-Ferritin Bioinorganic Nanocomposite," Science **269,** 54–57 (1995).

[13] B. Hennequin, L. Turyanska, T. Ben, A. Beltran, S. Molina, M. Li, S. Mann, A. Patane, and N. Thomas, "Aqueous Near-Infrared Fluorescent Composites Based on Apoferritin-Encapsulated PbS Quantum Dots," Adv. Mater. **20,** 3592–3596 (2008).

[14] N. Galvez, P. Sanchez, and J. Dominguez-Vera, "Preparation of Cu and CuFe Prussian Blue derivative nanoparticles using the apoferritin cavity as nanoreactor," Dalton Trans. p. 2492 (2005).

[15] J. Lopez-Castro, J. Delgado, J. Perez-Omil, N. Galvez, R. Cuesta, R. Watt, and J. Dominguez-Vera, "A new approach to the ferritin iron core growth: influence of the H/L ratio on the core shape," Dalton Trans. **41,** 1320–1324 (2012).

[16] U. Carmona, L. Li, L. Zhang, and M. Knez, "Ferritin light-chain subunits: key elements for the electron transfer across the protein cage," Chem. Commun. **50,** 15358–15361 (2014).

[17] I. Yamashita, K. Iwahori, and S. Kumagai, "Ferritin in the field of nanodevices," Biochim. Biophys. Acta. **1800,** 846–857 (2010).

[18] R. Watt, O. Petrucci, and T. Smith, "Ferritin as a model for developing 3rd generation nano architecture organic/inorganic hybrid photo catalysts for energy conversion," Catal. Sci. Technol. **3,** 3103–3110 (2013).

[19] D. Xu, G. Watt, J. Harb, and R. Davis, "Electrical Conductivity of Ferritin Proteins by Conductive AFM," Nano Lett. **5,** 571–577 (2005).

[20] J. Keyes, R. Hilton, J. Farrer, and R. Watt, "Ferritin as a photocatalyst and scaffold for gold nanoparticle synthesis," J. Nanopart. Res. **13,** 2563–2575 (2011).

[21] M. Pyon, R. Cherry, A. Bjornsen, and D. Zapien, "Uptake and Release of Iron by Ferritin Adsorbed at Tin-Doped Indium Oxide Electrodes," Langmuir **15,** 7040–7046 (1999).

[22] M. Tominaga, A. Ohira, Y. Yamaguchi, and M. Kunitake, "Electrochemical, AFM and QCM studies on ferritin immobilzed onto a self-assembled monolayer-modified gold electrode," J. Electoanal. Chem. **566,** 323–329 (2004).

[23] T. Mastsui, N. Matsukawa, K. Iwahori, K. Sano, K. Shiba, and I. Yamashita, "Direct Production of a Two-Dimensional Ordered Array of Ferritin-Nanoparticles on a Silicon Substrate," Jpn. J. Appl. Phys. **46,** L713–L715 (2007).

[24] M. Li and S. Mann, "DNA-directed assembly of multifunctional nanoparticle networks using metallic and bioinorganic biulding blocks," J. Mater. Chem. **14,** 2260–2263 (2004).

[25] I. Kim, H. Hosein, D. Strongin, and T. Douglas, "Photochemical reactivity of ferritin for Cr(VI) reduction," Chem. Mater. **14,** 4874–4879 (2002).

[26] T. Rakshit and R. Mukhopadhyay, "Tuning band gap of holoferrtin by metal core reconstitution with Cu, Co, and Mn," Langmuir **27,** 9681–9686 (2011).

[27] P. Yu and M. Cardona, *Fundamentals of Semiconductors*, 4th ed. (Springer, New York, 1998), pp. 268–273.

[28] G. Liu, S. Debnath, K. Paul, W. Han, D. Hausner, H. Hosein, F. Michel, J. Parise, D. Sparks, and D. Strongin, "Characterization and surface reactivity of ferrihydrite nanoparticles assembled in ferritin," Langmuir **22,** 9313–9321 (2006).

[29] M. Preisinger, M. Krispin, T. Rudolf, S. Horn, and D. Strongin, "Electonic structure of nanoscale iron oxide particles measured by scanning tunneling and photoelectron spectroscopies," Phys. Rev. B **71,** 165409 (2005).

[30] J. Colton, S. Erickson, T. Smith, and L. Moses, "Sensitive detection of surface- and size-dependent direct and indirect band gap transitions in ferritin," Nanotechnology **25,** 135703 (2014).

[31] B. Gilbert, C. Frandsen, E. Maxey, and D. Sherman, "Band-gap measurements of bulk and nanoscale hematite by soft x-ray spectroscopy," Phys. Rev. B **79,** 035108 (2009).

[32] N. Cherepy, D. Liston, J. Lovejoy, H. Deng, and J. Zhang, "Ultrafast studies of photoexcited electron dynamics in gamma- and alpha-Fe2O3 semiconductor nanoparticles," J. Phys. Chem. B **102,** 770–776 (1998).

[33] R. Hilton, B. Zhang, L. Martineau, G. Watt, and R. Watt, "Anion deposition into ferritin," J. Inorg. Biochem. **108,** 8–14 (2012).

[34] W. Shockley and H. Queisser, "Detailed Balance Limit of Efficiency of p-n Junction Solar Cells," J. Appl. Phys. **32,** 510–519 (1961).

[35] A. D. Vos, "Detailed balance lmit of the efficiency of tandem solar cells," J. Phys. D: Appl. Phys. **13,** 839–846 (1980).

[36] R. King *et al.*, "Solar cell generations over 40 percent efficiency," Prog. Photovolt: Res. Appl. **20,** 801–815 (2012).

[37] A. J. Nozik, "Quantum Dot Solar Cells," Phys. E. **14,** 115–120 (2002).

[38] S. Ruhle, M. Shalom, and A. Zaban, "Quantum-Dot-Sensitized Solar Cells," ChemPhysChem **11,** 2290–2304 (2010).

[39] S. Baskoutas and A. Terzis, "Size-dependent band gap of colloidal quantum dots," J. Appl. Phys **99,** 013708 (2006).

[40] M. Beard, A. Midgett, M. Hanna, J. Luther, B. Hughes, and A. Nozik, "Comparing Multiple Excition Generation in Quantum Dots to Impact Ionization in Bulk Semiconductors: Implications for Enhancement of Solar Energy Conversion," Nano Lett. **10,** 3019–3027 (2010).

[41] M. Hanna and A. Nozik, "Solar conversion efficiency of photovoltaic and photoelectrolysis cells with carrier multiplication absorbers," J. Appl. Phys. **100,** 074510 (2006).

[42] R. Schaller, M. Sykora, J. Pietryga, and V. Klimov, "Seven Excitons at a Cost of One: Redifining the Limits for Conversion Efficiency of Photons into Charge Carriers," Nano Lett. **6,** 424–429 (2006).

[43] S. Kim, W. Kim, Y. Sahoo, A. Cartwright, and P. Prasad, "Multiple exciton generation and electrical extraction from a PbSe quantum dot photoconductor," Appl. Phys. Lett. **92,** 031107 (2008).

[44] P. Santra and P. Kamat, "Tandem-Layered Quantum Dot Solar Cells: Tuning the Photovoltaic Response with Luminescent Ternary Cadmium Chalcogenides," J. Am. Chem. Soc. **135,** 877–885 (2013).

[45] M. Joo, G. Tourillon, D. Sayers, and E. Theil, "Rapid reduction of iron in horse spleen ferritin by thioglycolic acid measured by dispersive X-ray absorption spectroscopy," Bio Met.l **3,** 171–175 (1990).

[46] O. Lowry, N. Rosebrough, A. Farr, and R. Randall, "Protein measurement with the Folin phenol reagent," J. Biol. Chem. **193,** 265–275 (1951).

[47] C. Snow, L. Martineau, R. Hilton, S. Brown, J. Farrer, J. Boerio-Goates, B. Woodfield, and R. Watt, "Ferritin iron mineralization proceeds by different mechanisms in MOPS and imidazole buffers," J. Inorg. Biochem. **105,** 972–977 (2011).

[48] T. Smith, S. Erickson, C. M. Orozco, A. Fluckiger, L. Moses, J. Colton, and R. Watt, "Tuning the band gap of ferritin nanoparticles by co-depositing iron with halides or oxo-anions," J. Mater. Chem. A. **2,** 20782–20788 (2014).

[49] S. Erickson, T. Smith, L. Moses, R. Watt, and J. Colton, "Non-native Co-, Mn-, and Ti-oxydydroxide nanocrystals in ferritin for high efficiency solar energy conversion," Nanotechnology **26,** 015703 (2015).

[50] "AM1.5G Solar Spectrum," http://rredc.nrel.gov/solar/spectra/am1.5/ (Accessed July, 2014).

Index